NUREG/CR-4969
SAND87-1670
R1 and RD
Printed September 1987

Axisymmetric Analysis of a 1:6-Scale Reinforced Concrete Containment Building Using a Distributed Cracking Model for the Concrete

Joe R. Weatherby

Prepared by
Sandia National Laboratories
Albuquerque, New Mexico 87185 and Livermore, California 94550
for the United States Department of Energy
under Contract DE-AC04-76DP00789

Prepared for
U. S. NUCLEAR REGULATORY COMMISSION

Available from

Superintendent of Documents
U.S. Government Printing Office
Post Office Box 37082
Washington, D.C. 20013-7082

and

National Technical Information Service
Springfield, VA 22161

NUREG/CR-4969
SAND87-1670
R1 and RD

AXISYMMETRIC ANALYSIS OF A 1:6-SCALE REINFORCED CONCRETE CONTAINMENT BUILDING USING A DISTRIBUTED CRACKING MODEL FOR THE CONCRETE

Joe R. Weatherby

Sandia National Laboratories
Albuquerque, NM 87185
Operated by
Sandia Corporation
for the
U.S. Department of Energy

Prepared for
Mechanical/Structural Engineering Branch
Division of Engineering Technology
Office of Nuclear Regulatory Research
U.S. Nuclear Regulatory Commission
Washington, DC
Under Memorandum of Understanding DOE 40-550-75
NRC FIN No. A1401

ABSTRACT

Results of axisymmetric structural analyses of a 1:6 scale model of a reinforced concrete nuclear containment building are presented. Both a finite element shell analysis and a simplified membrane analysis were made to predict the structural response and ultimate pressure capacity of the model. Analytical results indicate that the model will fail at an internal pressure of 187 psig when the stress level in the hoop reinforcement at the midsection of the cylinder exceeds the ultimate strength of the bar splices.

Contents

List of Figures

List of Tables

ACKNOWLEDGEMENTS

Sincere appreciation is expressed to Dave Clauss, Chris Conley, and members of the Peer Review Panel on the NRC Containment Integrity Program for providing valuable suggestions and discussions related to the analytical effort. The work of Joe Jung, who made earlier contributions to the analytical effort, is also greatly appreciated. Thanks are also extended to Walt von Riesemann and Dan Horschel for the help they provided during the course of this work.

1. EXECUTIVE SUMMARY

Under a program sponsored by the U.S. Nuclear Regulatory Commission, Sandia National Laboratories has been investigating methods for predicting the structural response of nuclear reactor containment buildings subjected to loads produced by hypothetical severe accidents. As part of this program, a 1:6-scale reinforced concrete containment model will be pressurized to failure in 1987. Data generated by the test will serve as a benchmark for evaluating analytical methods used to predict the response, failure mode, and ultimate load capacity of similar containment structures. Ten organizations, including Sandia, have conducted pretest analyses of the containment structure. Many of the results from the pretest analysis effort are documented in [1]. This report describes additional calculations made at Sandia since the preparation of [1].

The 1:6-scale model was designed for an accident pressure of 46 psig following the requirements of the ASME Boiler and Pressure Vessel Code, Section III, Division 1 and 2. The firm responsible for the design and construction of the model was United Engineers and Constructors. The containment model is 22 feet in diameter and has a total height of 37 feet. A steel liner on the inner surface of the concrete wall serves as the pressure boundary for the structure. The primary reinforcement in the structure consists of #4 steel reinforcing bars. In addition to reinforcement oriented in the hoop and meridional directions, the model also contains reinforcement designed to carry seismic loads. The seismic reinforcement is oriented at 45° to the hoop and meridional directions.

Equipment hatches, pipes, and airlocks typically penetrate the containment wall in actual containment buildings. For this reason, representations of several types of penetrations were included in the 1:6-scale model. The model contains two equipment hatches and two personnel airlock representations. The model also contains two 8-inch diameter penetrations placed at locations in the cylinder wall diametrically opposed from one another and connected by a steel rod. The purpose of the rod is to simulate the effect of a large bore pipe that passes through the containment building and resists the radial expansion of the structure.

In the work reported here, both an axisymmetric finite element shell analysis of the containment structure and a membrane analysis of the cylinder midsection were conducted. The equipment hatches, personnel airlocks, and constrained penetrations were ignored in these models. These analyses differ from similar analyses reported in [2] in that distributed cracking models were used to represent the mechanical

behavior of the concrete in tension. In the previous finite element calculations, plasticity models were used for the concrete, and in the previous membrane analysis, the stiffness of the concrete was completely ignored. Results from the current membrane analysis were used as a point of reference for evaluating the results of the finite element calculations with concrete cracking. This comparison was necessary since the iterative solution technique employed in the nonlinear finite element analysis failed to reduce the force residuals to an acceptable level in many steps of the analysis. In spite of this fact, it is believed that this set of finite element calculations represents a more accurate prediction of the response of the structure than the results reported in [2].

In the membrane analysis of the cylinder midsection, hoop cracks formed at 42 psig internal pressure followed by the formation of meridional cracks and liner yielding at 110 psig. The hoop reinforcement at the cylinder midsection reached the yield point at 122 psig internal pressure followed by yielding of the seismic reinforcement at 130 psig and yielding of the meridional bars at 148 psig. The ultimate strength of the hoop reinforcement was reached at 183 psig.

Finite element results at the midsection of the cylinder were in close agreement with the results of the membrane analysis except for the prediction of the internal pressure necessary to cause yielding of the meridional reinforcement. An internal pressure of 167 psig was required to cause yielding of the meridional reinforcement in the cylinder midsection in the shell model, as compared to 148 psig in the membrane analysis. This discrepancy is believed to be due to convergence problems in the finite element solution. Based on the axisymmetric finite element shell analysis, the ultimate load capacity of the containment structure is predicted to be 187 psig. At this pressure, the hoop bars in the midsection of the cylinder reach the level of stress necessary to cause failure at splices in the reinforcing bars.

2. INTRODUCTION

The Containment Integrity Division at Sandia National Laboratories is currently involved in experimental and analytical programs to determine how accurately state-of-the-art analytical methods can be used to predict the structural response and ultimate load capacity of reinforced concrete reactor containment buildings subjected to loads resulting from a severe accident. As part of this program, a 1:6-scale model of a reinforced concrete containment building (see Fig. 1) has been constructed and will be pressurized to failure in July 1987. Ten organizations, including Sandia, have submitted predictions of the structural response of the containment model [1]. The data obtained from the overpressurization test will be compared to these analytical predictions.

Several of the pretest analyses of the containment structure conducted at Sandia are documented in [2]. The scope of the effort in [2] consisted of nonlinear axisymmetric shell and continuum analyses based on the finite element method as well as a simplified membrane analysis of the cylinder wall in which the stiffness of the concrete was neglected. In all of the previous finite element calculations, the concrete was assumed to behave as a non-hardening elastic-plastic material with different yield strengths in tension and compression. This type of material response was obtained by using the standard ABAQUS material model for concrete and suppressing the softening due to cracking and crushing. The ability of the concrete to carry tensile load decreases as cracking progresses, and, to simulate this phenomenon, two separate finite element analyses were conducted. In the first set of calculations, the tensile yield strength of the concrete was set equal to the experimentally measured ultimate strength of the concrete. The results from this analysis gave estimates of the structural response in the low pressure range where the concrete carries a significant fraction of the net tensile load. A second set of finite element calculations was conducted in which the yield strength of the concrete was set equal to a very small value (10 psi). The results from the second analysis gave estimates of the structural response in the high pressure range where the concrete in the dome and cylinder is heavily damaged and contributes very little to the overall stiffness of the structure. This two-step analytical approach was taken in order to avoid numerical difficulties associated with the sudden softening of the concrete after cracking or crushing.

The finite element analysis described in this report is based on the same finite element mesh used in the shell studies reported in [2]. Instead of treating the concrete as a non-hardening elastic-plastic material in both tension and compression, a distributed cracking model was used to represent the tensile behavior. The specific

constitutive model that was used in this analysis was the standard ABAQUS material model for concrete found in version 4-5-171 of the code (this is the same material option used in [2], but with a different set of material parameters). In this model, the concrete softens gradually after the initiation of cracking or crushing. Although extremely small pressure steps ($\approx$ .05 psig) were used to apply load to the structure, convergence problems were encountered in the solution. In spite of this problem, the finite element analysis described in this report is believed to provide a more accurate prediction of the response of the containment structure than the analyses reported in [2].

A nonlinear membrane analysis for the midsection of the cylinder wall was described in [2] in addition to the finite element analyses that were reported there. Originally, the membrane analysis was performed by writing and solving the equilibrium equations in terms of the stress in the steel liner and reinforcement, completely neglecting the stiffness of the concrete. In the more recent work described in this report, the membrane analysis has been modified to include the load carried by the concrete both before and after the initiation of cracking. The new membrane analysis provides a second set of results to compare against those obtained from the current finite element solution, which employs a distributed cracking model for the concrete. The results of the new membrane and finite element analyses are in close agreement with one another with regard to the predicted radial displacement of the cylinder wall and to the stress states in the liner and reinforcing steel at the midheight of the cylinder.

3. FAILURE CRITERIA

Realistic failure criteria must be adopted for all potential failure mechanisms in order to predict the ultimate pressure capacity of the containment. Failure is defined as any event which results in significant leakage. A high degree of uncertainty exists in selecting these failure criteria since, in many cases, the criteria are based on data derived from simple uniaxial tension and compression tests but are then applied to locations in the structure which are subject to more complex multiaxial loading conditions.

Except for regions where a large transverse shear force is present, the steel reinforcing bars are primarily in a state of uniaxial tension. Under this loading condition, the reinforcing bars are assumed to fail at a tensile stress level of 99 ksi (680 MPa). This value is based on results of tensile tests on spliced rebar specimens similar to those used in the construction of the 1:6-scale model. The containment structure is assumed to fail when the stress level in any layer of reinforcement in the

shell model reaches the ultimate strength of the bars.

Tearing of the liner constitutes another possible failure mode of the containment. The failure criterion used for the steel liner is based on equivalent plastic strain. Failure is assumed to occur when the equivalent plastic strain reaches the level of plastic strain at maximum load in a uniaxial tensile test. This value is approximately 15% for the liner material.

One of the most difficult modes of failure to evaluate or predict is failure brought on by radial shearing forces. When a crack develops through the concrete wall, the shearing force is transmitted by friction and aggregate interlock across the crack surfaces, and by dowel action of the reinforcing bars that span the crack plane. The models used to represent the rebar and concrete are too simplified to directly evaluate the potential for shear failure based solely on the material models and failure criteria for the steel and concrete. As an alternative, two empirical criteria were used as a basis for evaluating the shear strength of sections subject to combined shear and membrane tension. Experimental results [3] indicate that the ultimate strength of a reinforced concrete section in shear falls within the range

$$1.9\sqrt{f_c'} \leq \tau_u \leq 17\sqrt{f_c'} \tag{3.1}$$

where τ_u is the ultimate shear strength in units of psi and f_c' is the ultimate compressive strength of the concrete in psi. The failure criterion developed in [3] suggests that between the limits of Equation 3.1, the ultimate strength varies according to the relation

$$\tau_u = [.013\,(\rho f_y - \sigma_v) + 1.9]\sqrt{f_c'} \tag{3.2}$$

where

ρ = meridional reinforcement ratio = A_s/A_g
f_y = tensile yield strength of the steel, psi.
σ_v = P_m/A_g
A_s = area of steel in meridional direction, sq. in.
A_g = total area of the containment wall in meridional direction, sq. in.
P_m = force in the meridional direction, lb.

The area of the liner is not included in calculating A_s or A_g; likewise, the meridional force carried by the liner is not included in P_m. A second criterion based on the shear-friction model [4] was also used to estimate the ultimate shear strength between the limits in Equation 3.1. The shear-friction model states that the shear strength varies according to

$$\tau_u = \rho f_y - \sigma_v \tag{3.3}$$

When the radial shear force, V, is such that V/A_g exceeds either of the two values calculated for τ_u from Equations 3.2 and 3.3, then the probability of a shear failure is considered to be high.

4. MEMBRANE ANALYSIS

The major assumption made in the membrane analysis of the cylinder wall presented in [2] is that strains due to bending are negligible so that the state of strain is uniform through the wall thickness. The addition of concrete to the membrane analysis is straightforward, and the equilibrium equations become

$$\sigma_h s_h n_h A + \tfrac{1}{2}\sigma_s s_s n_s A + t_l \sigma_l^h + t_c \sigma_c^h = pR \tag{4.1}$$

$$\sigma_m s_m n_m A + \tfrac{1}{2}\sigma_s s_s n_s A + t_l \sigma_l^m + t_c \sigma_c^m = \frac{pR}{2} - \frac{W}{2\pi R} \tag{4.2}$$

where

$\sigma_h, \sigma_s, \sigma_m$ = axial stresses in the hoop, seismic, and meridional bars

n_h, n_s, n_m = number of layers of hoop, seismic, and meridional bars

s_h, s_s, s_m = number of bars per unit length in the direction perpendicular to the bar in the hoop, seismic, and meridional layers

σ_l^h, σ_l^m = liner stresses in the hoop and meridional directions, respectively

σ_c^h, σ_c^m = concrete stresses in the hoop and meridional directions, respectively

t_l, t_c = liner thickness and concrete thickness, respectively

A = cross-sectional area of each bar

R = cylinder radius

W = weight of the containment above the cylinder midheight

p = internal pressure

The concrete is assumed to remain linearly elastic until either the hoop or meridional stress exceeds the ultimate strength of the concrete. The ultimate strength of the concrete in tension is denoted by f_t'. When the concrete stress in a given direction reaches f_t', the material is assumed to crack. The nomenclature used to identify cracks is such that the plane of a *hoop crack* runs parallel to the axis of revolution for the cylinder, and the plane of a *meridional crack* runs perpendicular to the axis of revolution for the cylinder. In the membrane analysis, a hoop crack is formed when the hoop stress reaches f_t', and a meridional crack is formed when the meridional stress reaches f_t'. Further straining in the direction normal to the plane of the crack is assumed to result in a linear decrease of the stress component normal to the

crack plane. Each stress component in the concrete is assumed to vanish when the corresponding strain component reaches the yield strain of the reinforcing steel. The analysis is simplified by neglecting the Poisson effect so that the stress-strain relation for the concrete in the hoop direction is given by

$$\sigma_c^h = \begin{cases} E_c \epsilon_h & \text{if } \epsilon_h < f_t'/E_c \\ \left(1 - \dfrac{\epsilon_h - f_t'/E_c}{\epsilon_y - f_t'/E_c}\right) f_t' & \text{if } f_t'/E_c < \epsilon_h < \epsilon_y \\ 0 & \text{if } \epsilon_h > \epsilon_y \end{cases}$$

where E_c is the Young's modulus of the concrete, ϵ_h is the hoop strain, and ϵ_y is the yield strain of the reinforcing steel. A similar stress-strain relationship is used in the meridional direction.

The descending branch of the concrete stress-strain curve is used to account for the so-called "tension stiffening" effect which can be observed in data from tensile tests on reinforced concrete panels [5]. This term refers to the fact that even after cracks form in the panel, the concrete between cracks will continue to carry load and contribute to the stiffness of the panel. Test results suggest that the stiffening effect of the concrete tends to disappear as the average strain normal to the crack plane reaches the yield strain of the reinforcing steel.

Material properties used for the rebar are listed in Table 1. The cross-sectional area, A, of each rebar is taken to be 0.2 in^2 which corresponds to the nominal area of a standard #4 steel bar. For the membrane analysis, the steel liner was treated as an elastic-plastic material with a Young's modulus of 30×10^6 psi, a yield strength of 50.2 ksi, and a hardening modulus of 2.56×10^5 psi. The Young's modulus of the concrete, E_c, was taken to be 4.8×10^6 psi, and a value of 500 psi was used for f_t' based on results of direct and split tension tests. Values of .0625 in and 9.75 in were assumed for the thicknesses of the liner and concrete, respectively.

As in [2], the equilibrium equations were solved using a modified Newton method. A listing of the current version of the FORTRAN program[1] used in the solution of the equations is provided in Appendix A. Figure 2 shows a plot of the stresses in each reinforcement layer as a function of pressure. These results were generated by

[1] In addition to changes made to incorporate concrete into the membrane analysis, two coding errors in the original version of the program used in [2] were also corrected. These errors were related to the calculation of the equivalent plastic strain in the liner and had a relatively minor effect on the predicted response. For internal pressures above that necessary to cause liner yielding, the corrections shifted the pressure-displacement results by approximately 7 psig with displacements being larger in the corrected version of the code for a given value of internal pressure. The weight of the containment structure above the midheight of the cylinder was also corrected from the previous value of $.221 \times 10^6$ lb to $.16 \times 10^6$ lb. This correction did not result in a significant change in the results of the membrane analysis.

incrementally increasing the pressure in steps of 2 psig. Equilibrium iterations were continued during each pressure step until the norm of the out-of-balance forces was less than 1×10^{-5} of the norm of the applied forces. The analysis predicts that hoop cracks form at 42 psig followed by the formation of meridional cracks and liner yielding at 110 psig. The hoop reinforcement reaches yield at an internal pressure of 122 psig followed by yielding of the seismic reinforcement at 130 psig, and by yielding of the meridional bars at 148 psig. The analysis was terminated at 183 psig when the hoop reinforcement reached the stress level necessary to cause failure of the bar splices (99 ksi).

5. FINITE ELEMENT SHELL ANALYSIS

The finite element mesh used for the axisymmetric shell analyses reported in [2] was also used in the present analysis. Figure 3 shows an outline of this mesh. Two-noded, thick-shell elements are used throughout the model. Nine integration points were used to integrate through the thickness of the shell, and single-point integration was used along the length of each shell element. The basemat is assumed to rest on a rigid surface, and interface elements were placed between the basemat and rigid surface to allow for uplift of the basemat. The present analysis will be referred to as Model 5 to distinguish it from the previous shell analyses in [2] which are denoted as Models 1 and 2, and the continuum analyses in [2] which are denoted as Models 3 and 4.

The layered shell and rebar options in the ABAQUS code were used to place the liner and rebar at the appropriate positions through the thickness of the shell. Material properties for the reinforcing steel and liner material are listed in Tables 1 through 3. The nominal values for liner thickness listed in Tables 2 and 3 were used in the analysis rather than the actual values. The measured thicknesses of the liners are approximately 9% less than the nominal thicknesses reported in the construction drawings; however, this discrepancy was not discovered until after the analysis had been completed. This difference is not expected to have a significant impact on the predicted response of the structure.

The transverse shear stiffness of the thick-shell element in the ABAQUS computer code remains constant throughout the analysis and is by default set equal to $\frac{5}{6}G_c t_c$, where G_c is the initial shear modulus of the concrete layer and t_c is the thickness of the concrete layer. In contrast, the transverse shear stiffness of the containment wall will change significantly after cracking of the concrete. Since we are primarily interested in the response of the containment after the onset of cracking, the transverse shear stiffness of the shell was set equal to $\frac{1}{6}G_c t_c$ which corresponds

to the transverse shear stiffness of a linear elastic shell having a shear modulus equal to 20% of the shear modulus of the uncracked concrete.

The concrete constitutive model in the ABAQUS code was used to represent the concrete in the containment model. This material model is capable of describing both cracking and crushing of the concrete. The constitutive model requires input of several parameters, including points from the stress vs. plastic strain curve in uniaxial compression, the uniaxial tensile strength, the biaxial compressive strength, the magnitude of plastic strain at failure in uniaxial tension, and the magnitude of the plastic strain at failure under biaxial compression. Points used to define a piecewise linear relationship between the uniaxial compressive stress and the equivalent plastic strain are listed in Table 4, and values for the remaining material parameters are listed in Table 5. The ABAQUS default values were used for those parameters requiring biaxial test data since this information was not available. To account for the tension stiffening effect, the concrete constitutive model allows the user to define an unloading curve for the concrete after cracking in tension. In this analysis, the component of stress normal to the crack plane is assumed to decrease linearly with increasing strain, finally vanishing when the difference between the total strain component normal to the crack plane and the normal strain component at the onset of cracking is equal to the yield strain of the reinforcing steel ($\approx 0.2\%$).

The dead load due to the weight of the concrete was applied in the first step of the analysis. This load was applied as a body force of .086 lb/in^3 acting downward. In addition, the weight of the one foot thick concrete fill slab which rests on top of the basemat was accounted for by applying a downward pressure load of 1.6 psi to the basemat liner. Following the application of the gravity load, the internal pressure was increased from 0 to 30 psig in six steps using automatic load incrementation. Between 30 psig and 170 psig, the pressure loading was increased directly using pressure increments of 0.041 psig. Pressure increments of 0.05 psig were used between 170 psig and 200 psig. Three equilibrium iterations were allowed in each increment for pressures above 30 psig. If the convergence was not achieved within three iterations, the analysis was continued to the next pressure increment. The solution time for the problem was 4.6 cpu hours on a Cray X-MP/24.

Convergence in the ABAQUS program is determined by comparing the maximum force residual to a convergence tolerance specified by the user. This tolerance is usually defined to be a small fraction of a typical nodal force which is applied to the structure. A convergence tolerance of 2.5×10^3 lb was used throughout the analysis. At 30 psig, the specified convergence tolerance was 15% of a typical nodal force applied in the cylinder region and .14% of the vertical load carried by the cylinder. At 200 psig the value of the specified convergence tolerance was 2% of a typical nodal force applied in the cylinder region and 0.02% of the vertical load carried in

the cylinder region.

The convergence tolerance was met at each increment in the analysis up to a pressure of 97 psig. Between 97 psig and 98 psig, the maximum residuals associated with the vertical degrees-of-freedom near the base of the cylinder were approximately 2×10^4 lb, exceeding the specified tolerance. The convergence tolerance was again met for all increments between 98 psig and 112 psig. At 112 psig the residual force associated with a vertical degree-of-freedom near the midheight of the cylinder had a value of 8×10^5 lb. Following this, the convergence tolerance was again met for all load steps between 113 psig and 125 psig. At 125 psig, however, the residual associated with a vertical degree-of-freedom in the upper part of the cylinder exceeded the tolerance. Between 126 and 131 psig, the convergence criteria was satisfied. Above 131 psig, except for the pressure range from 168 psig to 172 psig, convergence was not achieved in most of the remaining load steps. At 180 psig, the strain in the hoop reinforcement near the cylinder midheight exceeded the strain necessary to cause splice failure in the rebar. Since this corresponds to the last data point entered for the rebar stress-strain curve, the results for pressures above 180 psig were ignored. The force residuals in the range of pressure from 126 psig to 180 psig were typically less than 1×10^5 lb, and the maximum force residuals were generally associated with the vertical degrees-of-freedom in the cylinder wall.

It is not possible to fully assess the effect of the residual forces on the predicted response of the containment solely on the basis of results from a single finite element analysis. The best way to determine an acceptable convergence tolerance for the force residuals is to run multiple analyses with successively tighter tolerances and compare the results. This approach was not followed because of the large amount of computer time required for each analysis. In the current analysis, the tolerance was chosen so that the maximum residual force would be small relative to a typical applied force. Even though the specified convergence tolerance was not met at each step in the current analysis, two observations lend some credibility to the finite element results presented here. First, the finite element results correspond closely with the membrane theory results with regard to the radial displacement in the midsection of the containment. This correlation will be shown later in the report. Second, for those load steps in which the tolerance was not met, the maximum force residual was generally associated with a vertical degree of freedom in the cylinder region. For these cases, the residual force was still small relative to the tensile load carried in the cylinder.

The cracking sequence of the concrete is described in Figures 4 through 9. These figures show the development of both hoop and meridional cracks at the inner surface, outer surface, and midthickness of the concrete mat and wall. Each symbol denotes a crack at an element integration point. The first crack in the concrete appeared at an

internal pressure of 35 psig in the meridional direction. This initial crack was located at the base of the cylinder, on the inside surface of the containment. At 38 psig, hoop cracks formed in the midsection of the cylinder. By 43 psig most of the cylinder was cracked in the hoop direction. Hoop and meridional cracks had formed in most of the dome region by 70 psig. Meridional cracks began to appear on the lower surface of the basemat at 104 psig, followed by the formation of hoop cracks at this location at 108 psig. The midsection of the cylinder cracked in the meridional direction at an internal pressure of 112 psig. Meridional cracks reached the midthickness of the basemat at 154 psig, and hoop cracks had developed at the midthickness by 157 psig.

A sequence of deformed shape plots of the containment structure are presented in Figure 10 for three different levels of internal pressure. Figures 11 and 12 contain plots of the radial displacement at the midheight of the cylinder as a function of pressure and present a comparison of the results from the current finite element analysis (Model 5) to those from the membrane analysis with concrete cracking and to the results of the finite element shell analyses described in [2] (Models 1 and 2). The radial displacements predicted by the membrane analysis are in close agreement with the results of Model 5 for the entire range of internal pressure. Figure 13 shows the vertical displacement of the dome apex as a function of pressure as predicted by the three finite element shell analyses. The uplift of the basemat beneath the cylinder wall is shown in Figure 14 for Models 1, 2, and 5. Here, the uplift is measured relative to the point where the axis of symmetry intersects the basemat. The basemat in Model 5 is more flexible since the concrete is allowed to soften following cracking whereas, in Models 1 and 2, the concrete was not allowed to soften after the yield surface was reached.

The distribution of stress in the rebar layers is shown in Figures 15 through 24. Figure 15 shows that at 125 psig a significant amount of the hoop reinforcement in the cylinder has reached the yield point (66.6 ksi), and that by 180 psig the hoop bars have reached the stress level necessary to initiate a splice failure (99 ksi). The largest stress in the Layer 2 meridional bars occurs in the first element above the basemat. Although some of the discontinuities in the curves in Figure 16 are the result of terminations of the meridional rebars, the stress discontinuities in the central section of the containment are thought to be the result of convergence difficulties which occur when the strains in the meridional direction approach the level at which the meridional stress in the concrete vanishes (at this point the unloading branch of the curve for the concrete has a discontinuity in slope). Figures 19 through 24 show that none of the reinforcement in the basemat reaches the yield point prior to 180 psig.

Figure 25 shows the stresses in the hoop, meridional, and seismic reinforcement at the midsection of the cylinder as a function of pressure. Although not shown in the figure, the liner yields at 110 psig at this location. The hoop bars reach yield at a

pressure of 124 psig followed by yielding of the seismic bars at a pressure of 132 psig, and yielding of the meridional bars at 167 psig. At 180 psig, the hoop bars reach the stress level at which splice failure occurs. With the exception of the stress in the meridional reinforcement between 130 and 160 psig, there is good agreement between the membrane theory results and the finite element results. The unloading seen in the outer meridional bars for pressures between 140 psig and 160 psig is believed to be the result of numerical problems. For this reason, the membrane theory results are considered to be more accurate than the finite element results for predicting the stress in the meridional reinforcement in the cylinder midsection between 140 psig and 160 psig.

Figures 26 and 27 show the fraction of the applied load carried in the various structural elements at the midheight of the cylinder. The concrete initially carries 86% of the load in hoop direction and 88% of the load in the meridional direction. The fraction of the load carried by the concrete in the hoop direction vanishes when the hoop bars reach yield at 124 psig, and, similarly, the load carried by the concrete in the meridional direction goes to zero when the meridional bars yield at 167 psig internal pressure. Before the concrete cracks, the liner carries 4% of the total load in the hoop direction and 6% in the meridional direction. At higher pressures ($>$ 130 psig) the liner carries approximately 20% of the total load in both the hoop and meridional directions. Note that the liner generally carries a larger share of the applied load than the seismic reinforcement in each of the two directions.

Figure 28 shows the stress in the meridional and seismic reinforcement at the base of the cylinder as a function of pressure. At this location, the inner meridional reinforcement (Layer 2) yields at a pressure of 125 psig followed by yielding of the Layer 10 meridional reinforcement at 132 psig and yielding of the outer meridional reinforcement (Layer 5) at 150 psig. The outer seismic bars (Layer 8) are in a state of compression over the whole pressure range. Figure 28 implies that the neutral axis of the shell is located between the inner and outer seismic reinforcement for pressures above 147 psig so that only a small part of the total cross-section at the base of the shell is in meridional compression.

The distribution of equivalent plastic strain in the liner is shown in Figure 29 for internal pressures ranging from 150 psig to 180 psig. At 180 psig, when the hoop bars in the midsection of the cylinder are predicted to fail, the maximum value of equivalent plastic strain in the liner is less than 6%. This is well below the plastic strain level of 15% which exists when the ultimate tensile strength of the liner material is reached in uniaxial tension and suggests that a liner failure is unlikely prior to the failure of the hoop bars in the cylinder midsection. This analysis, however, does not account for strain concentrations in the liner which may occur near cracks in the concrete wall so that liner rupture prior to 180 psig still remains a possibility. In

addition, more work is needed to establish a more reliable rupture criterion for the liner under biaxial loading conditions.

Bending at the base of the cylinder resulted in crushing of the concrete on the outer surface of the containment. This is demonstrated by plots of the hoop and meridional stresses shown in Figures 30 through 32. In the first element at the base of the cylinder, the meridional stress on the outer surface of the containment reaches a maximum value at 145 psig (see Fig. 30). From this point, the concrete begins to soften and completely loses all load carrying capacity at 166 psig. By comparison, the concrete at the same location in the Model 2 analysis reached the compressive yield surface at 145 psig internal pressure. The plots in Figure 31 show the meridional and hoop stresses on the outer surface in the second element above the base of the cylinder. This figure clearly reveals a deficiency in the constitutive model for the concrete. At 180 psig when the hoop stress is nearly zero, the meridional stress in the concrete reaches a value of -14500 psi which is far greater than the uniaxial compressive strength of 6800 psi.

The concrete on the outer surface of the dome adjacent to the springline began to crush at 175 psig. This crushing was brought about by bending at the springline induced by the mismatch in the radial stiffness of the dome and cylinder. By 180 psig, the region of crushing extended from the springline to a point 70 inches away from the springline along the surface of the dome.

The moment-curvature relationship at the base of the cylinder is shown in Figure 33 for the Model 5 analysis. The slope of this curve is always positive, indicating that a bending instability does *not* develop in the present analysis. This contradicts the speculation made in [2] that the containment will fail due to a bending instability at this location. Since the current analysis is considered to provide a better characterization of the concrete than the analyses in [2], the bending instability is no longer considered to be the most probable failure mode.

Figure 34 shows the radial shear force in the cylinder and dome regions. As expected, peaks occur at the basemat/cylinder junction, springline, and at the edge of the dome plates near the apex of the dome. The average radial shear stress existing at these locations is shown in Figure 35 as a function of internal pressure. The criteria used to determine the potential for radial shear failure are contained in Equations 3.1 through 3.3. The minimum shear strength of a section is assumed to be equal to $1.9\sqrt{f'_c}$, where f'_c is the ultimate compressive strength of the concrete. The shear stress in the dome near the springline and near the dome plates remain well below the minimum value of radial shear strength as shown in Figure 35. At 170 psig, the radial shear strength at the base of the cylinder is calculated to be 850 psi based on Equation 3.2 and 680 psi based on Equation 3.3. Both values are much larger than

the value of radial shear stress predicted by the finite element analysis at 170 psig at the base of the cylinder wall.

6. CORRECTION OF RESULTS TO ACCOUNT FOR WALL THICKNESS

When a pressure load is applied to an axisymmetric shell element in the ABAQUS code, the nodal forces are computed based on the radial position of the nodes which make up the shell element. These forces are directly proportional to the distance from the nodes to the axis of symmetry. In the finite element model of the containment structure, the nodes for each shell element were placed at the centerline of the containment wall. Hence, the pressure applied to the dome and cylinder wall in the finite element analysis is equivalent to a slightly higher pressure acting on the inner surface of the containment wall. The equivalent internal pressure, p_i, acting on the inner surface of the cylinder can be computed from the applied pressure, p, through the relation:

$$p_i = p\left(1 + \frac{t}{2R_i}\right) \tag{6.1}$$

where t is the thickness of the cylinder wall and R_i is the internal radius of the cylinder. This same correction should also be applied to the membrane theory results since the value used for R in Equations 4.1 and 4.2 was equal to the radius at the midthickness of the cylinder wall. The correction in Equation 6.1 shifts the predicted failure pressure of the containment from 180 psig to 187 psig. It should be noted that since this is a geometrically linear analysis, the applied nodal forces are not calculated based on the internal dimensions of the deformed structure.

7. CONCLUSION

Results of a membrane and axisymmetric finite element shell analysis of the containment structure have been presented. These analyses differ from previous analyses reported in [2] in that they allow for softening of the concrete following cracking or crushing. The softening behavior makes it far more difficult to obtain a converged finite element solution, and force residuals at the end of each load step were, in many cases, considerably larger than those existing in the shell analyses reported in [2]. In spite of this fact, the finite element analysis presented here is believed to provide a better estimate of the structural response of the containment than the previous analyses because the material model more accurately reflects the stiffness of the concrete.

Table 6 contains a summary of the important structural events which occur

during pressurization of the finite element model. An upper bound for the ultimate pressure capacity of the containment is 187 psig. At this pressure, the splices in the hoop bars reach their ultimate strength. The crushing of the concrete at the base of the cylinder region occurs at virtually the same pressure as in the Model 2 analysis of [2]. The moment-curvature relationship at this location in the current model (Model 5) indicates that the section can continue to carry an increasingly larger bending moment and that a limit point is not reached before 187 psig as was speculated in [2] (see Fig. 33). Shear failures and liner tearing prior to 187 psig also appear unlikely based on the failure criteria which have been adopted. Hence, based on the results presented in this report, the most likely mode of failure for the containment appears to be failure of the splices in the hoop bars at the midheight of the cylinder at an internal pressure of 187 psig.

8. REFERENCES

1. D. B. Clauss (ed.), *Round-Robin Pretest Analyses of a 1:6-Scale Reinforced Concrete Containment Model Subject to Static Internal Overpressurization*, Sandia National Laboratories, Albuquerque, New Mexico, NUREG/CR-4913, SAND87-0891, April 1987.

2. J. R. Weatherby, "SNL Pretest Analyses," in *Round-Robin Pretest Analyses of a 1:6-Scale Reinforced Concrete Containment Model Subject to Static Internal Overpressurization*, D. B. Clauss (ed.), Sandia National Laboratories, Albuquerque, New Mexico NUREG/CR-4913, SAND87-0891, April 1987, pp.40-81.

3. Y. Aoyagi and K. Yamada, "An Experimental Approach to the Design of Network Reinforcement Against In-Plane Shear in Reinforced Concrete Containments," *Proceedings of the 5th International Conference on Structural Mechanics in Reactor Technology*, Paper J4/7, 1979.

4. A. H. Nilson (ed.), *Finite Element Analysis of Reinforced Concrete*, American Society of Civil Engineers, 1982, p.264.

5. J. Eibl, U. Neuroth, F. -H. Schlüter, "Reinforced Concrete Elements Subjected to Uniaxial and Biaxial Direct Tension," Institut für Massivbau und Baustofftechnologie, Universität Karlsruhe, November 1986.

Table 1: Rebar Material Properties Based on Nominal Cross-Sectional Areas

Engineering Stress (ksi.)	(MPa.)	Plastic Strain
66.6	459	0.
73.3	505	.0094
85.6	590	.0200
99.0	683	.0430
Young's Modulus = 31×10^6 psi. (214×10^3 MPa.)		
Poisson's Ratio = .3		
Yield Strength = 66.6 ksi. (459 MPa.)		

Table 2: Material Properties for Dome Liner.

Engineering Stress (ksi.)	(MPa.)	Plastic Strain
51.4	354	0.
61.1	421	.0230
66.9	461	.0478
70.5	486	.0977
71.0	490	.1476
Young's Modulus = 30×10^6 psi. (207×10^3 MPa.)		
Poisson's Ratio = .3		
Yield Strength = 51.4 ksi. (354 MPa.)		
Nominal Thickness = .0833 in. (.212 cm.)		
Actual Thickness = .090 in. (.229 cm.)		

Table 3: Material Properties for Cylinder and Basemat Liner

Engineering Stress (ksi.)	(MPa.)	Plastic Strain
50.2	346	0.
50.2	346	.0157
59.0	407	.0308
66.0	455	.0696
68.0	469	.0937
70.0	483	.1620

Young's Modulus = 30×10^6 psi. (207×10^3 MPa.)
Poisson's Ratio = .3
Yield Strength = 50.2 ksi. (346 MPa.)
Nominal Thickness = .0625 in. (.159 cm.)
Actual Thickness = .068 in. (.173 cm.)

Table 4: Stress-Strain Data for Concrete Under Uniaxial Compression

Engineering Stress (ksi)	Plastic Strain
1.0	0.
2.0	3.33×10^{-5}
3.0	9.50×10^{-5}
3.9	1.88×10^{-4}
5.0	3.58×10^{-4}
6.8	5.83×10^{-4}
6.79	8.83×10^{-4}
3.4	3.44×10^{-3}

Table 5: Additional Material Parameters Used With the Concrete Constitutive Model in the ABAQUS Code.

PARAMETER DESCRIPTION	VALUE
Young's Modulus	4.8×10^6 psi.
Poisson's Ratio	.2
Ratio of each non-zero stress component at failure under biaxial compression to the stress magnitude at failure under uniaxial compression.	1.16‡
Ratio of the stress at failure under uniaxial tension to the stress at failure under uniaxial compression.	7.35×10^{-2}
Ratio of the magnitude of a component of plastic strain at failure under biaxial compression to the plastic strain at failure under uniaxial compression.	1.28‡
Ratio of the magnitude of plastic strain at failure under uniaxial tension to the plastic strain at failure under uniaxial compression.	.09‡

‡default value in ABAQUS code

Table 6: History of Events from the Model 5 Shell Analysis

PRESSURE‡ (psig)	EVENT
35	Meridional crack forms at the base of the cylinder on the inner surface.
38	Hoop cracks form at the midsection of the cylinder.
70	Hoop and meridional cracks develop in most of the dome region.
104	Meridional cracks appear on the lower surface of the basemat.
108	Hoop cracks appear on the lower surface of the basemat.
110	Liner yields in the midsection of the cylinder.
112	Meridional cracks form in the midsection of the cylinder.
124	Hoop reinforcement in the midsection of the cylinder yields.
125	Inner meridional reinforcement yields at the base of the cylinder.
132	Layer 10 meridional reinforcement yields at the base of the cylinder. Seismic reinforcement yields in the midsection of the cylinder.
150	Outer meridional reinforcement (Layer 5) yields at the base of the cylinder.
154	Meridional cracks develop at the midthickness of the basemat.
157	Hoop cracks develop at the midthickness of the basemat.
167	Meridional reinforcement yields in the midsection of the cylinder.
180	Stress in the hoop reinforcement near the midsection of the cylinder reaches the level necessary to cause extensive failure of the splices. This is the predicted failure mode of the containment.

‡the correction in Equation 6.1 has not been applied to these values

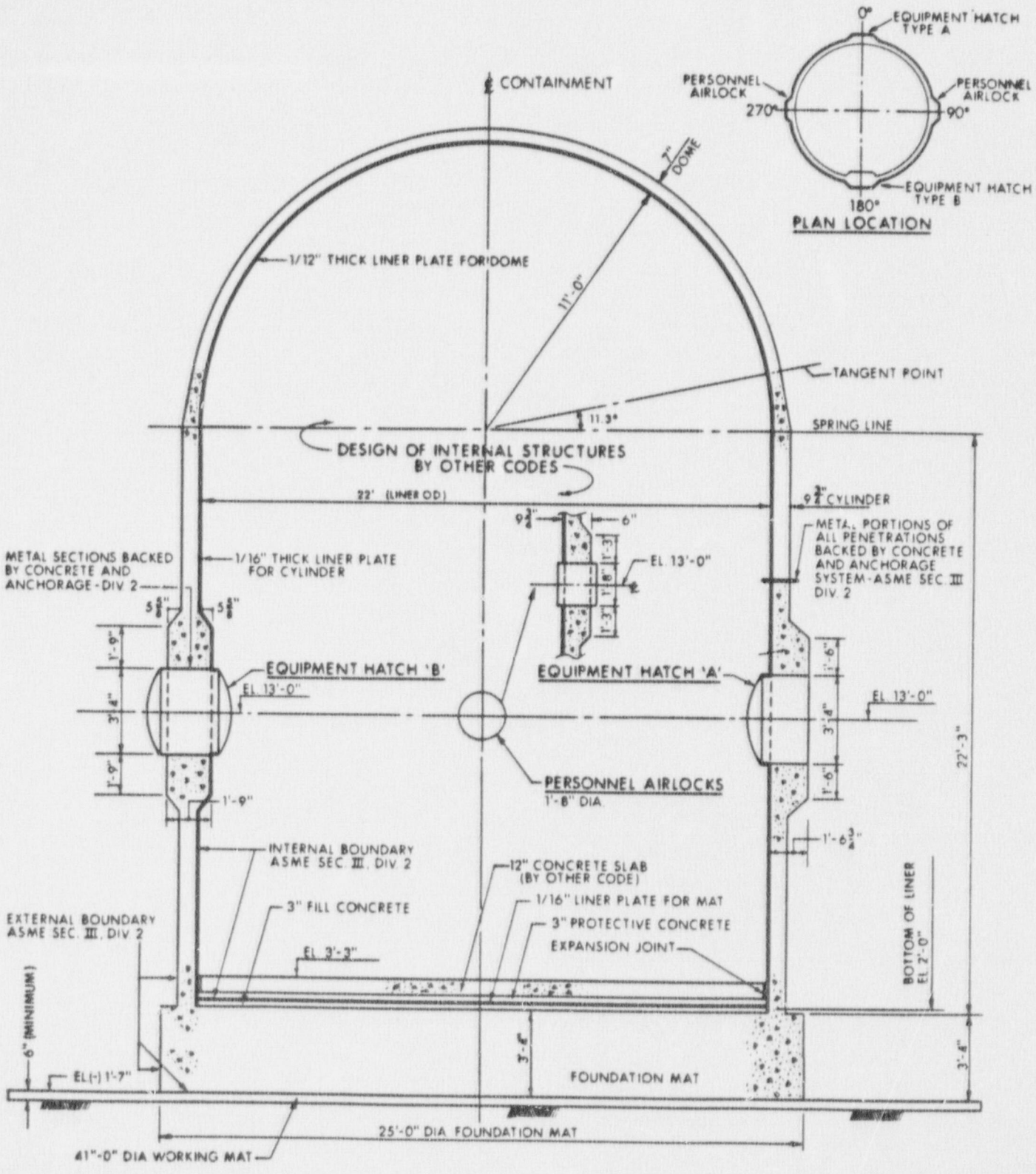

FIGURE 1. Layout of the 1/6th-scale Concrete Containment Model.

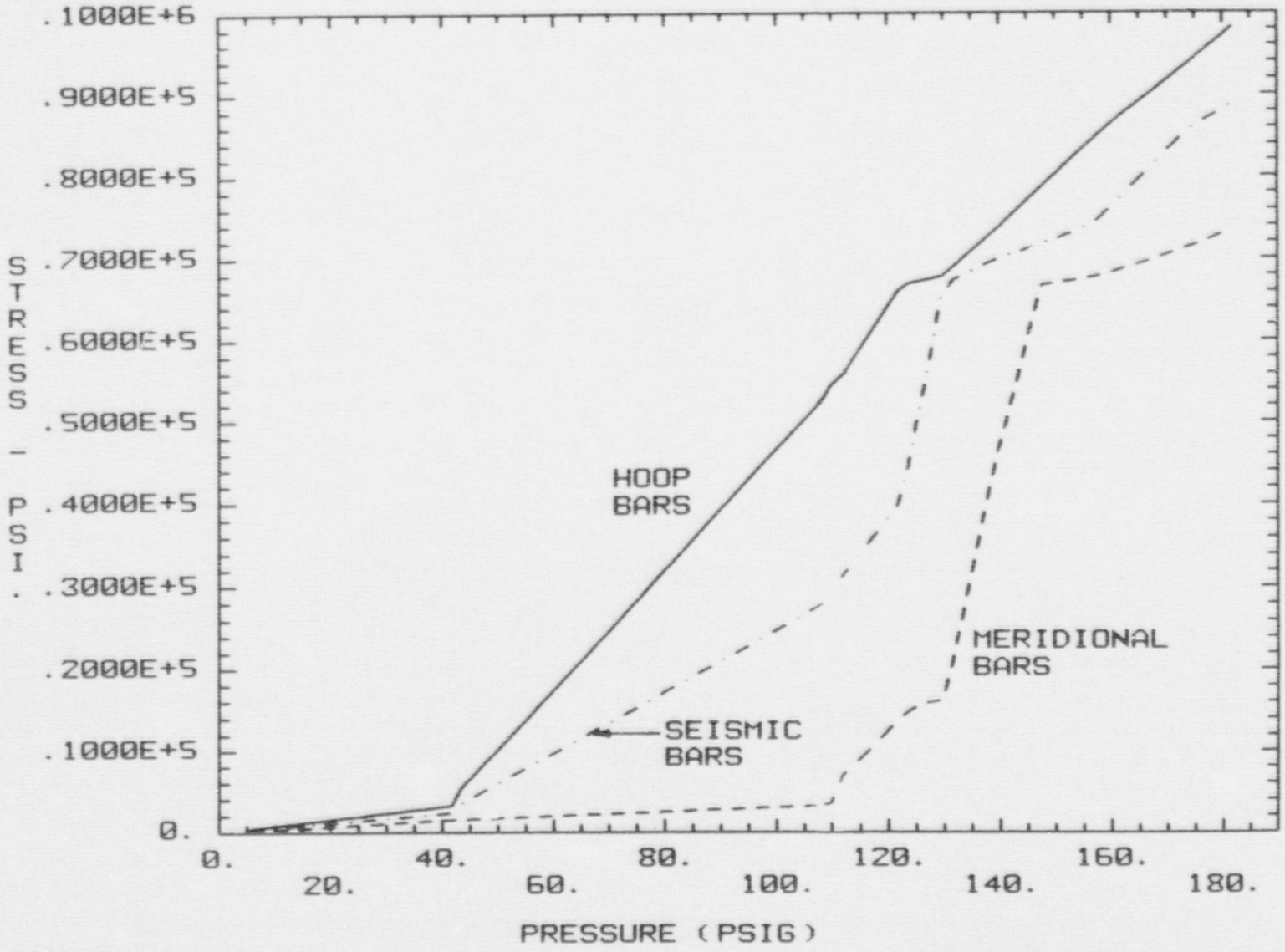

Figure 2. Stress in the Reinforcing Steel as a Function of Pressure at the Midheight of the Cylinder. Results are from the Membrane Analysis that Includes Concrete Cracking.

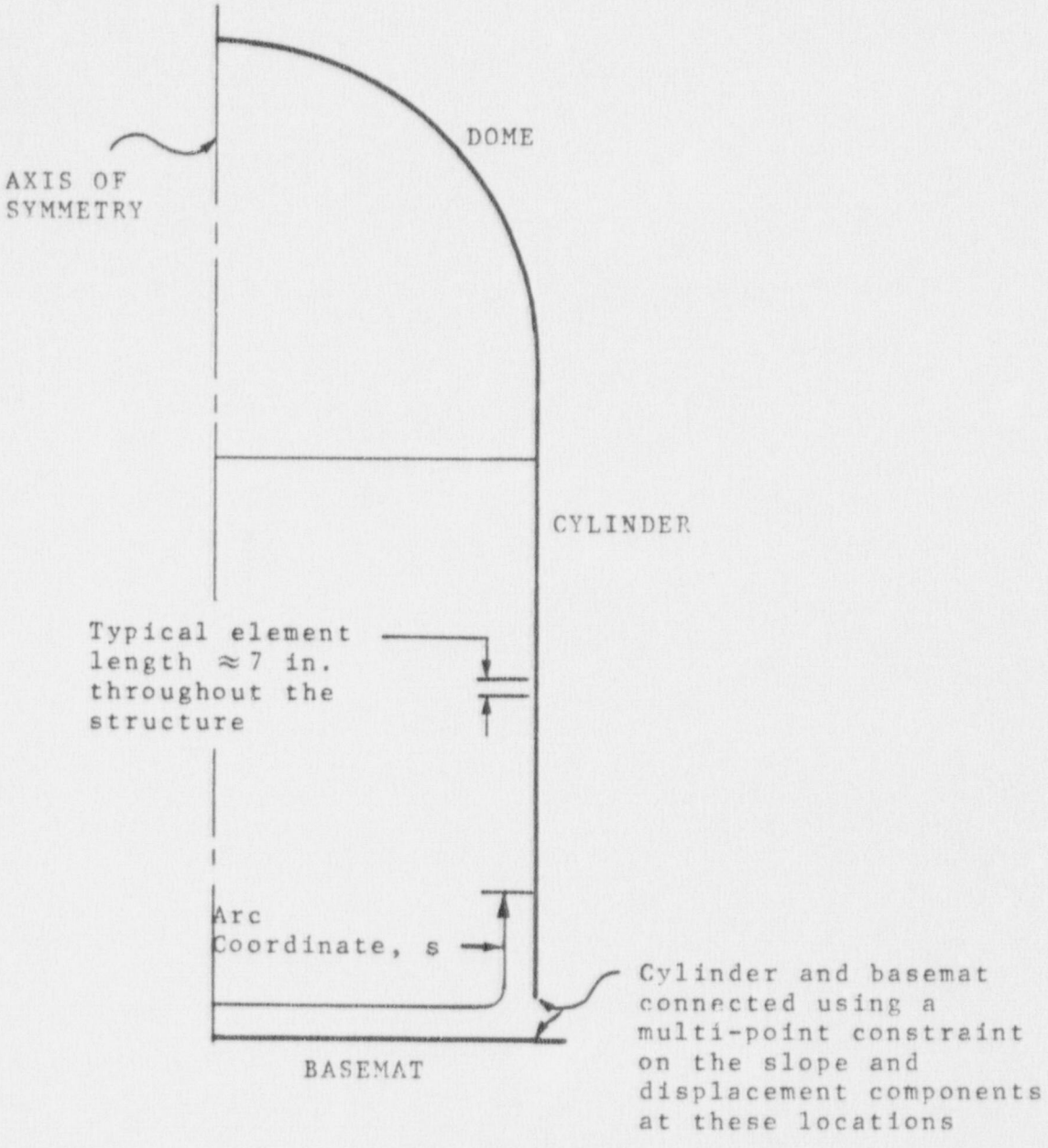

Figure 3. Outline of the Axisymmetric Finite Element Shell Model used in the Model 5 Analysis. The Arc Coordinate, s, is used in Spatial Plots of the Analysis Results

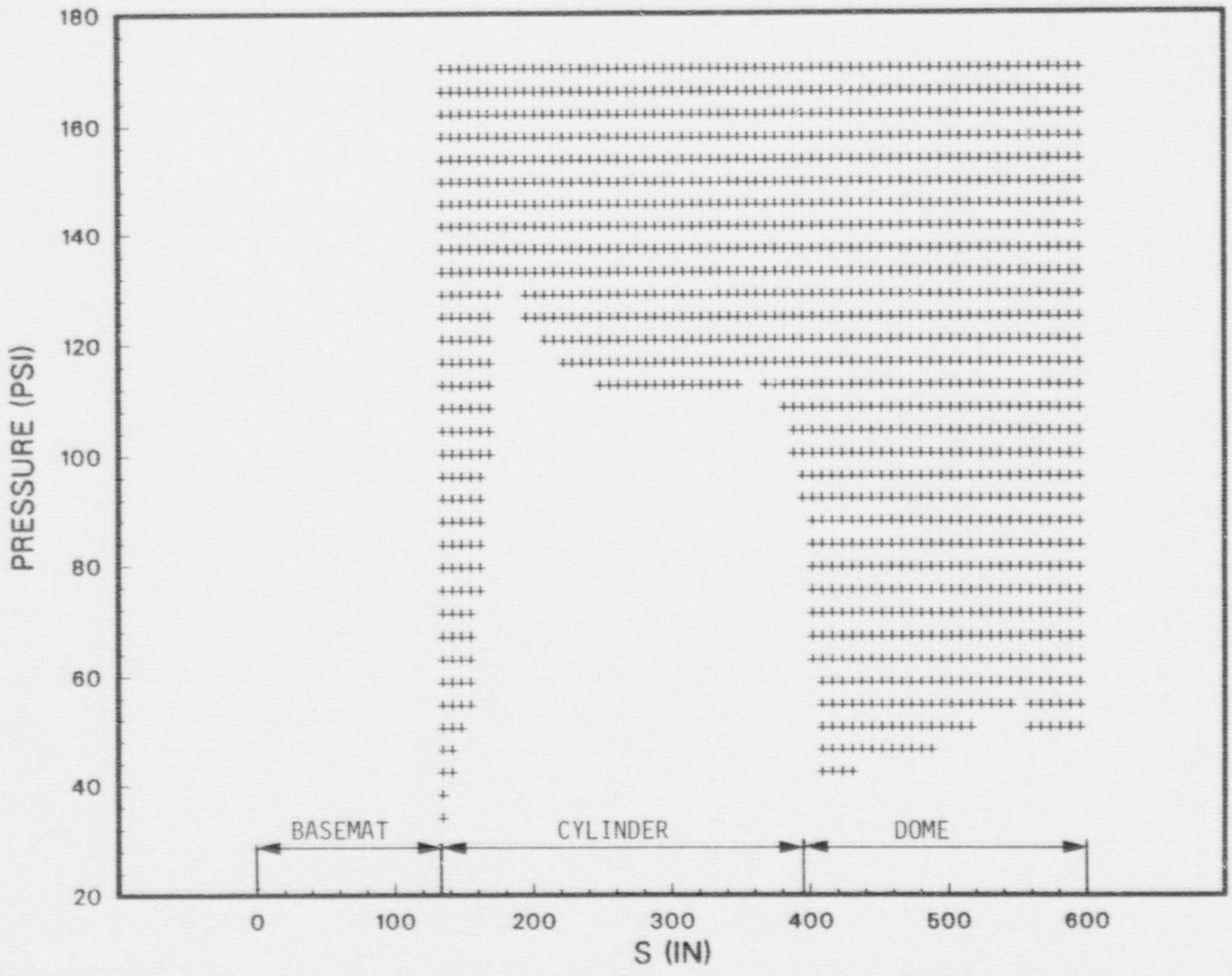

Figure 4. Development of Meridional Cracks on the Inner Surface of the Containment. Each Symbol Denotes a Crack at an Integration Point. (Model 5 Results)

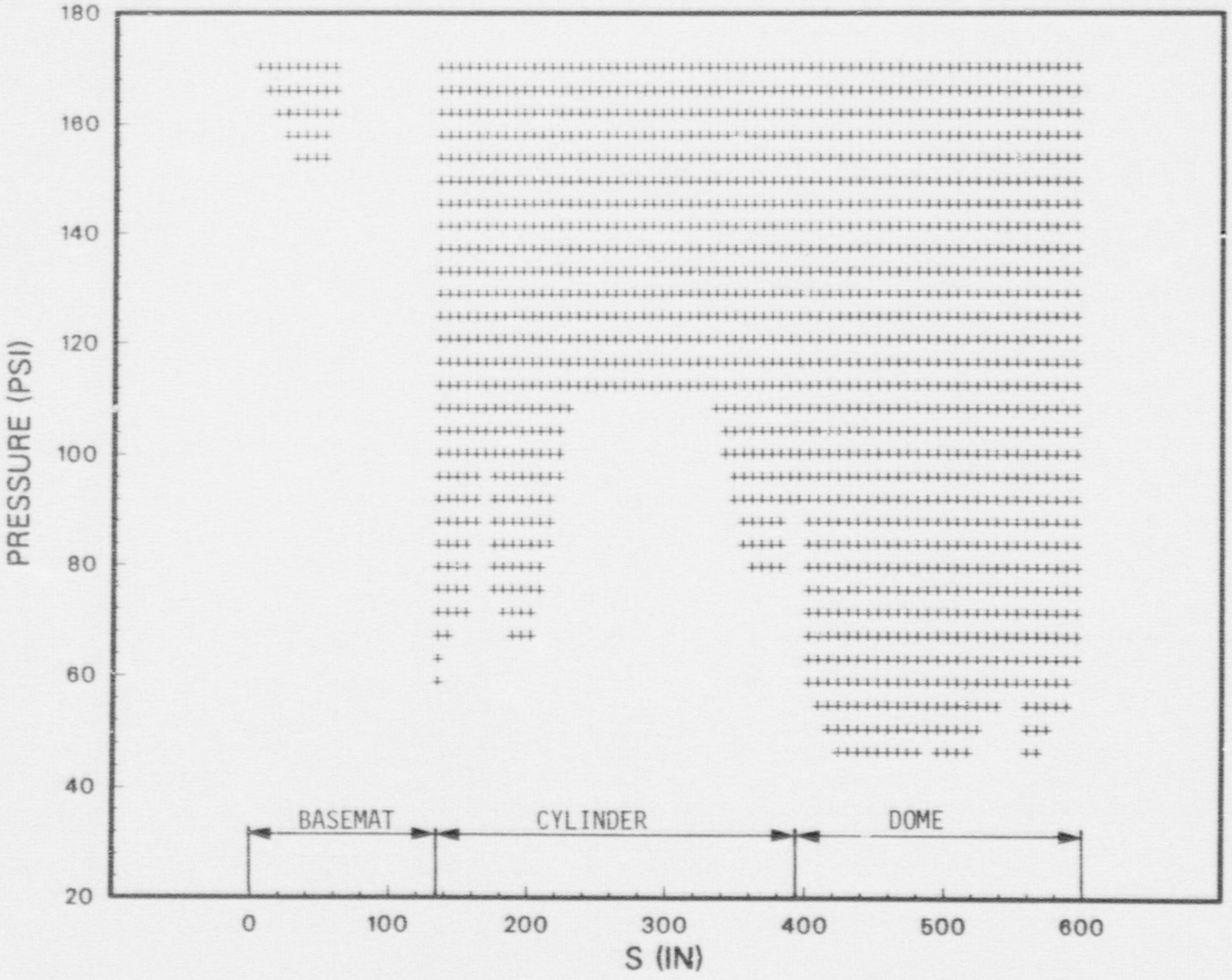

Figure 5. Development of Meridional Cracks at the Midthickness of the Containment. Each Symbol Denotes a Crack at an Integration Point. (Model 5 Results)

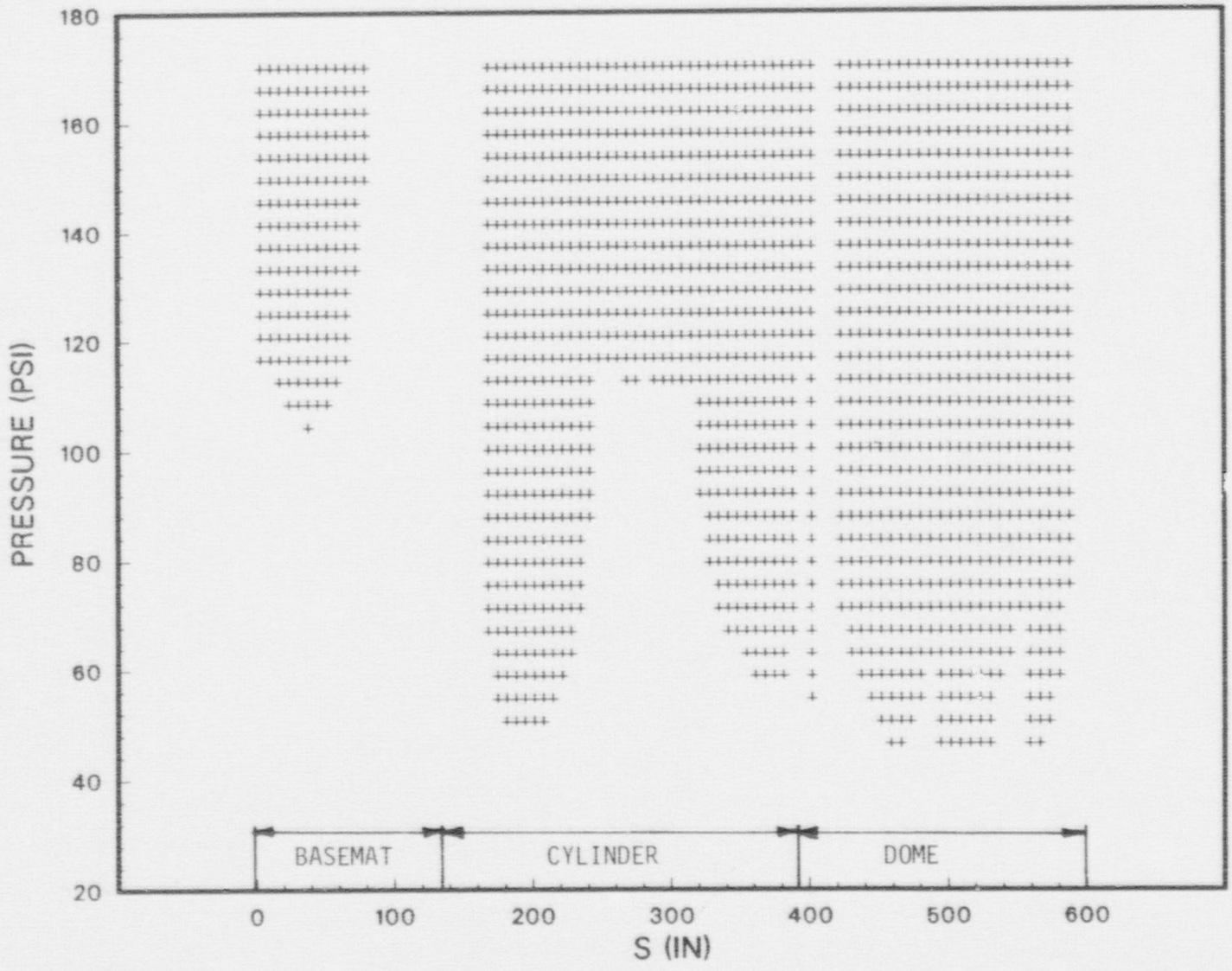

Figure 6. Development of Meridional Cracks on the Outer Surface of the Containment. Each Symbol Denotes a Crack at an Integration Point. (Model 5 Results)

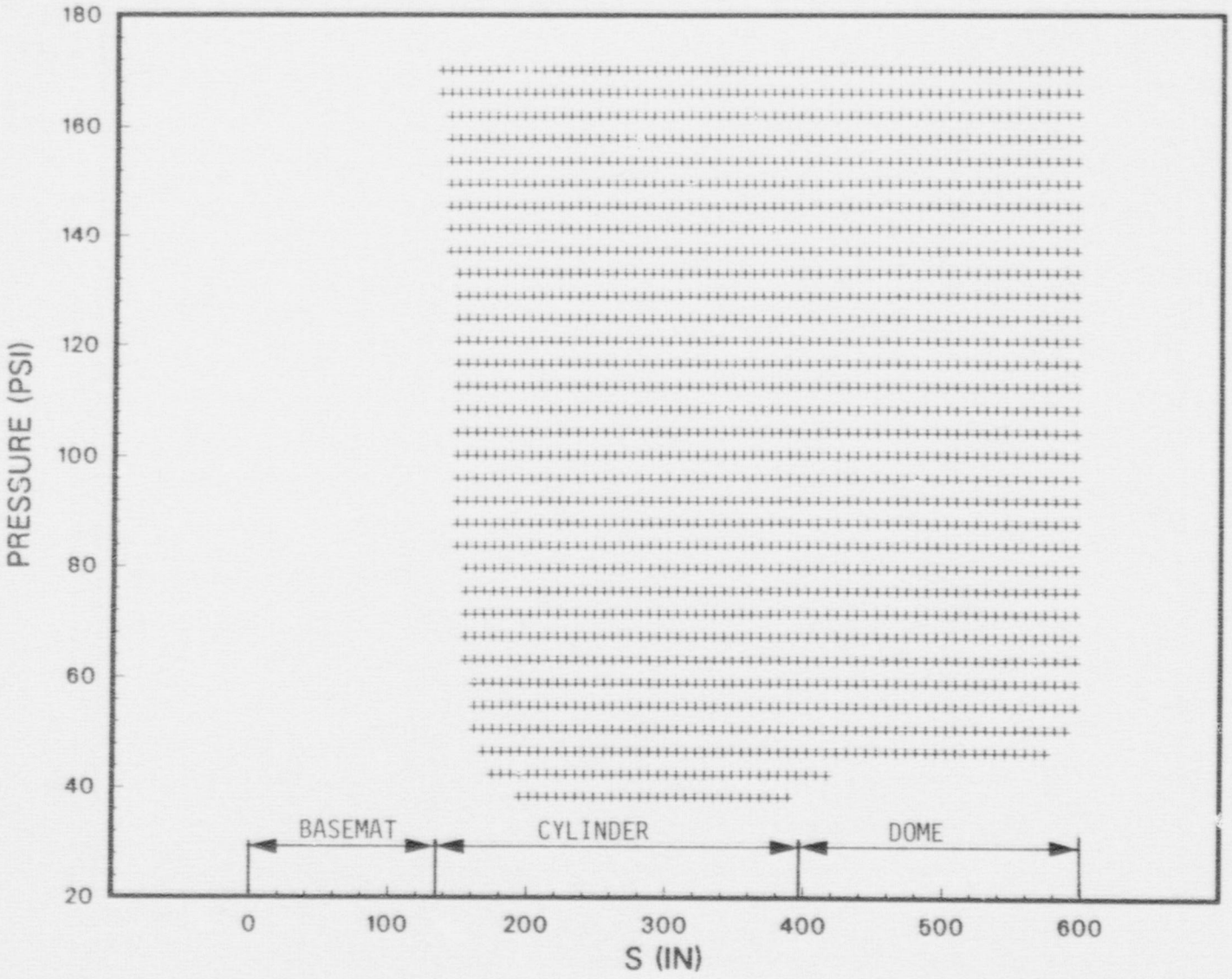

Figure 7. Development of Hoop Cracks on the Inner Surface of the Containment. Each Symbol Denotes a Crack at an Element Integration Point. (Model 5 Results)

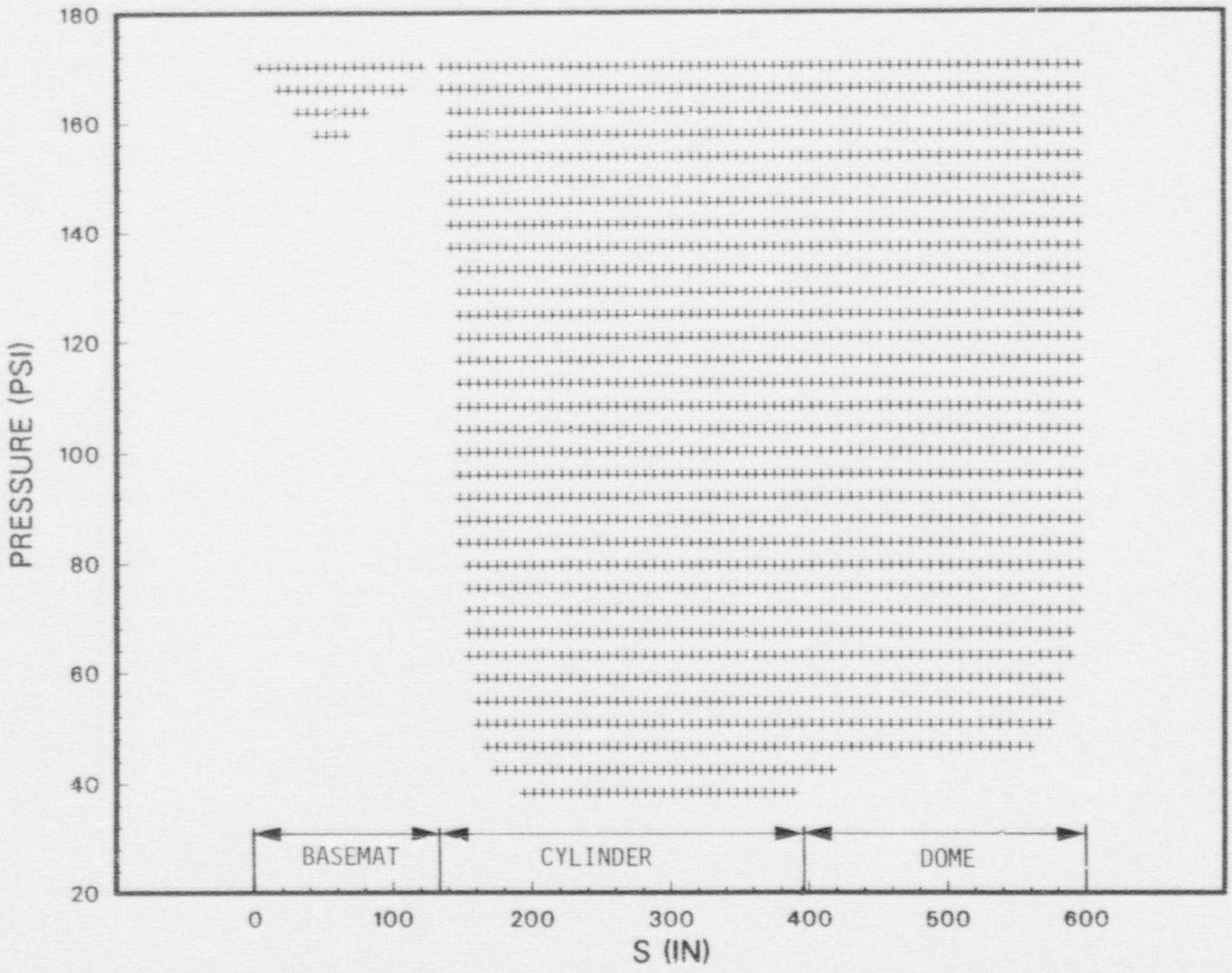

Figure 8. Development of Hoop Cracks at the Midthickness of the Containment. Each Symbol Denotes a Crack at an Integration Point. (Model 5 Results)

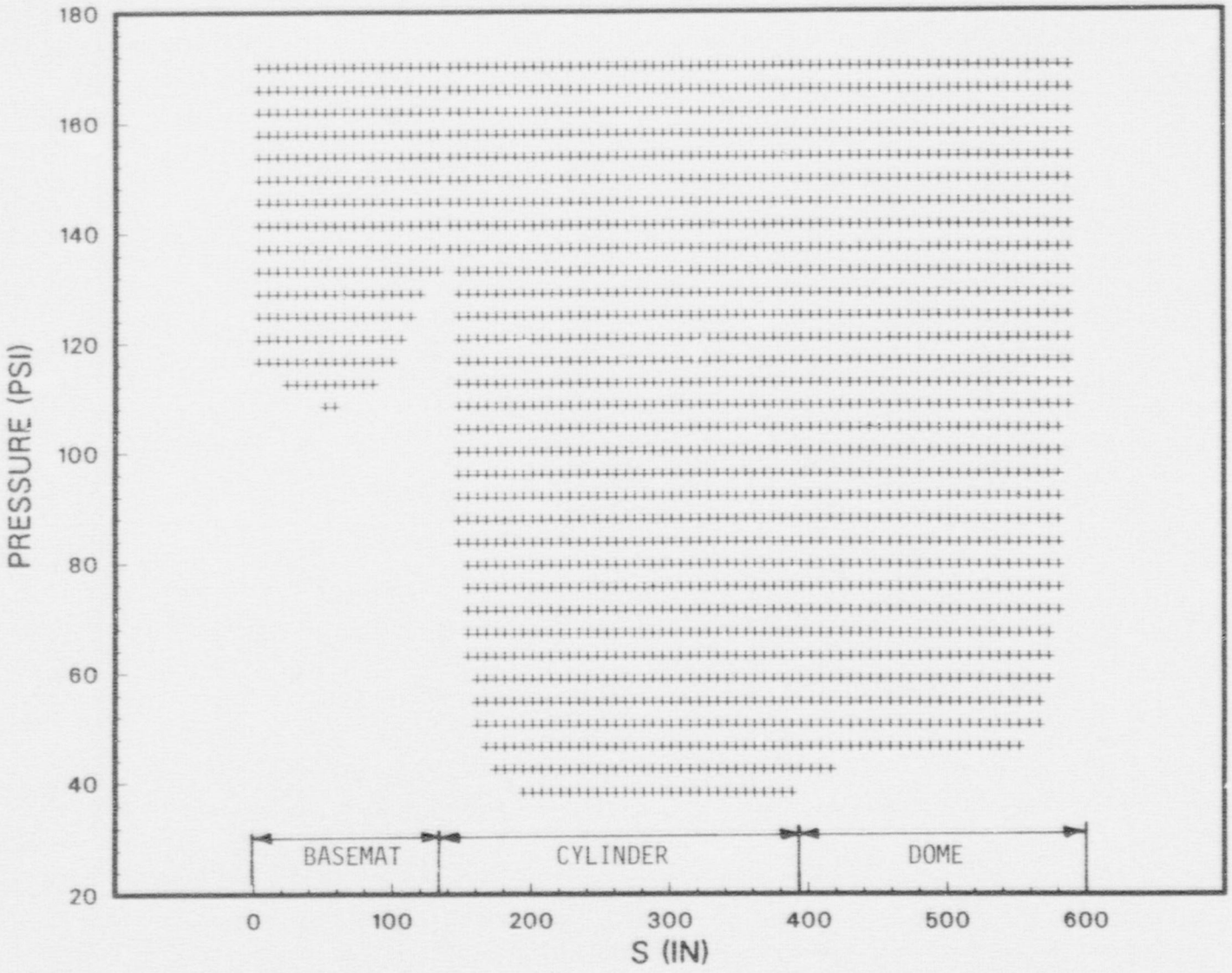

Figure 9. Development of Hoop Cracks on the Outer Surface of the Containment. Each Symbol Denotes a Crack at an Integration Point. (Model 5 Results)

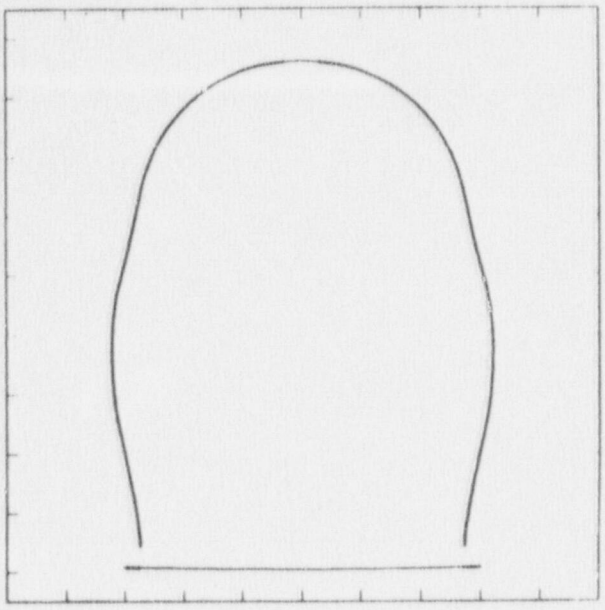

(a) Pressure = 145 psig

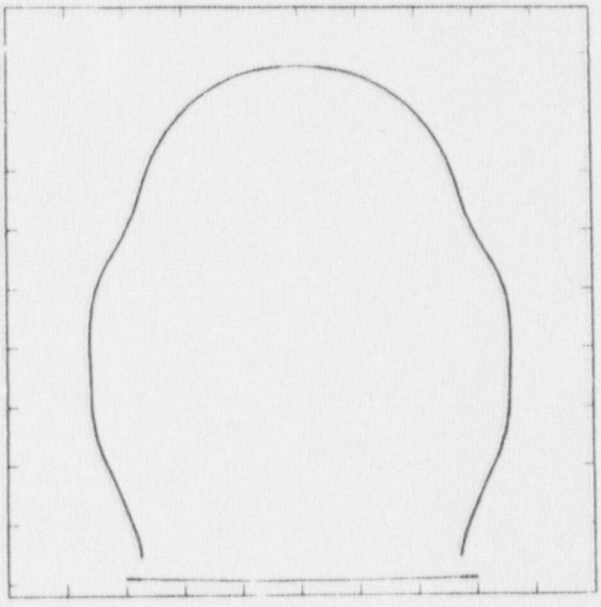

(b) Pressure = 166 psig

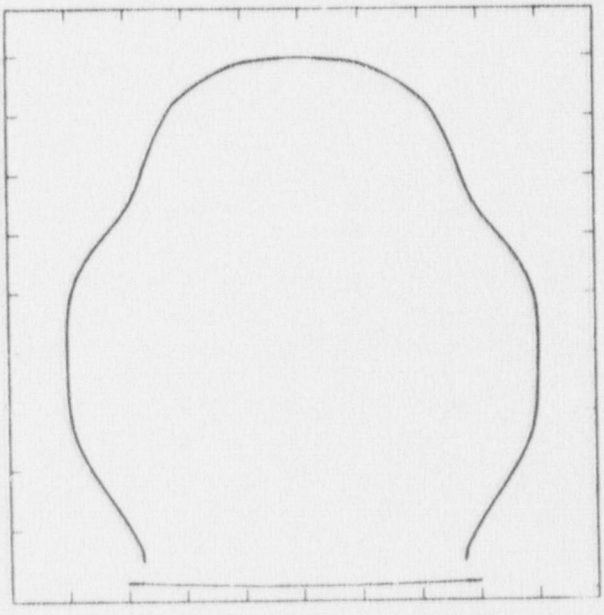

(c) Pressure = 180 psig

Figure 10. Deformed Shape Plots from the Model 5 Analysis at Internal Pressures of 145, 166, and 180 psig. The Magnification Factor for Displacements is 10

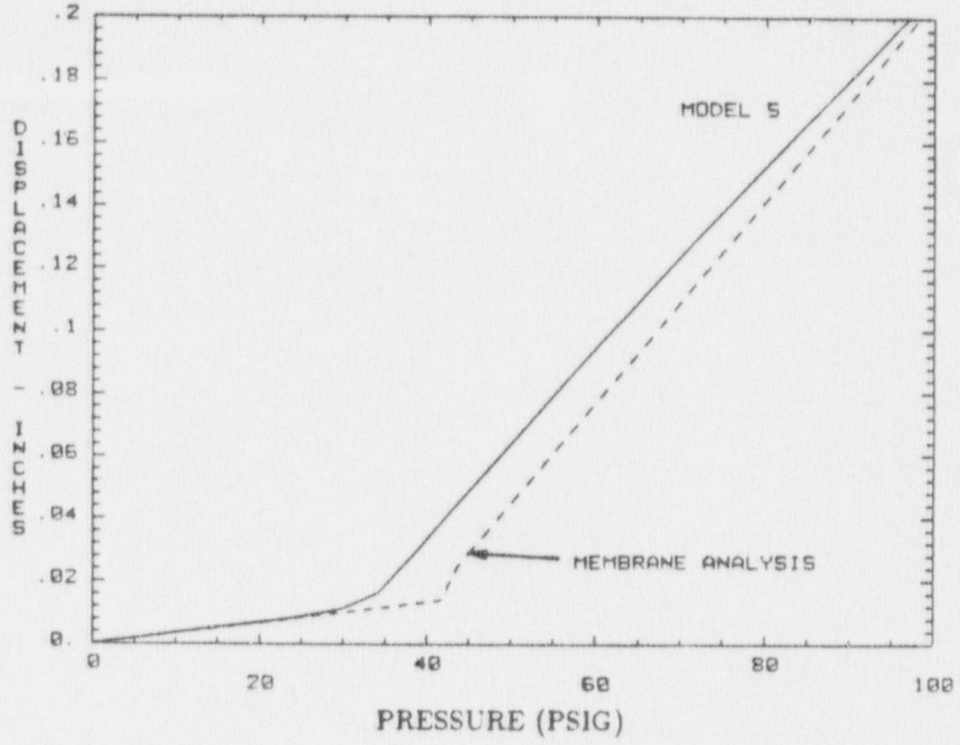

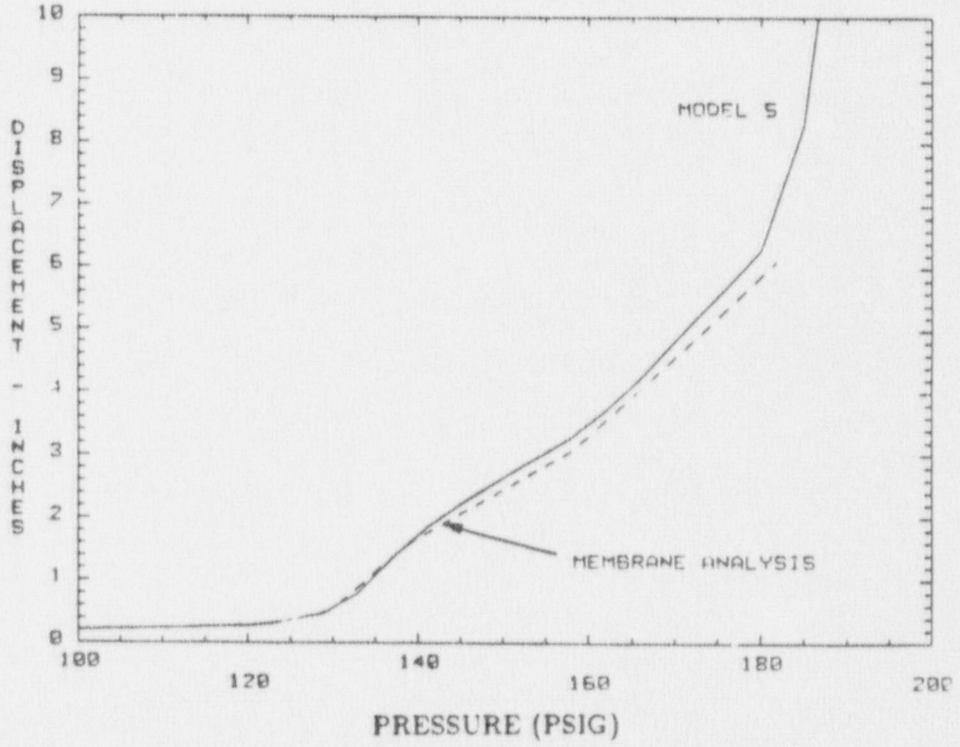

Figure 11. Radial Displacement at the Midheight of the Cylinder as a Function of Pressure from the Model 5 Shell Analysis and the Membrane Analysis with Concrete Cracking

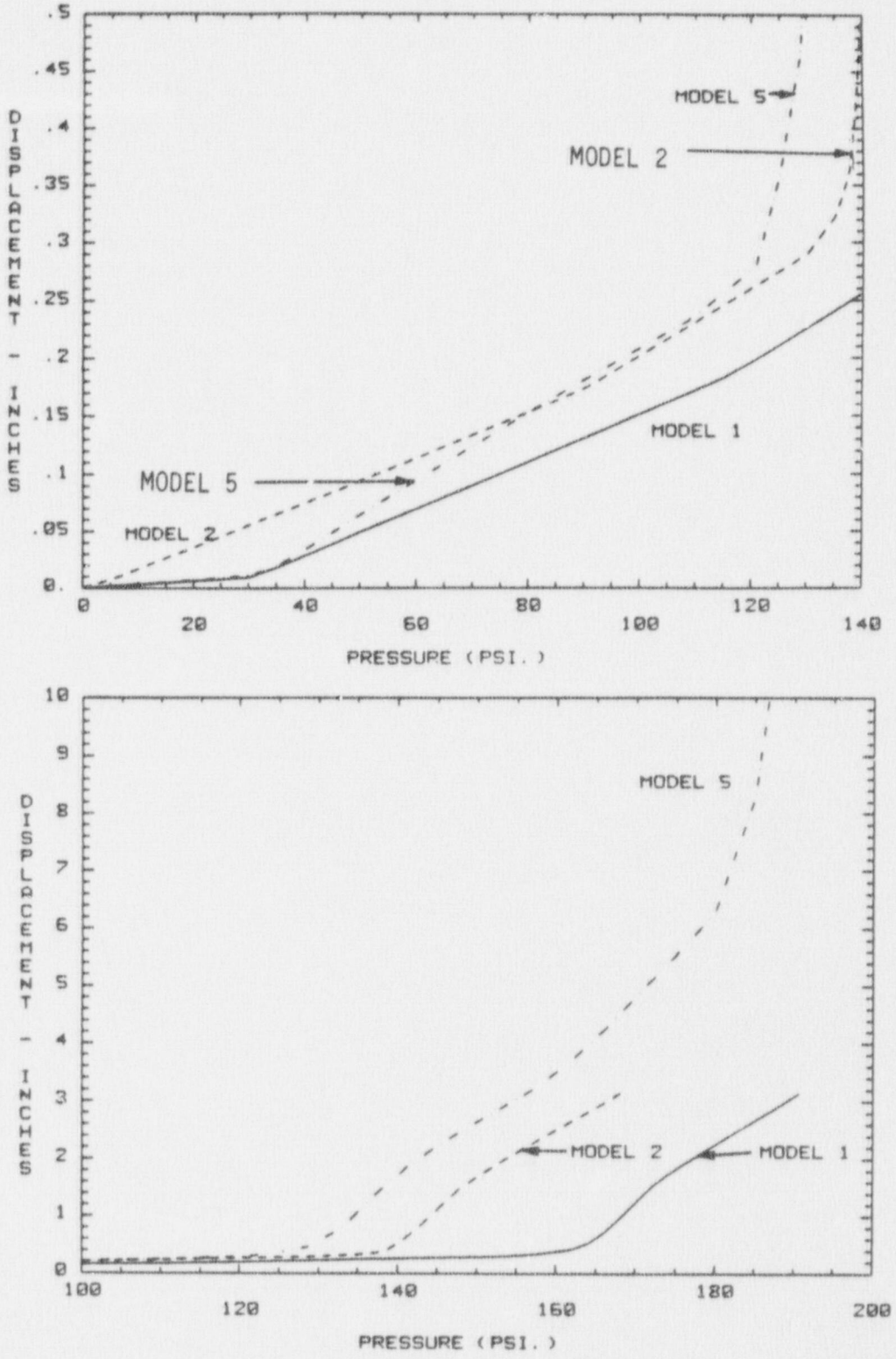

Figure 12. Radial Displacement at the Midheight of the Cylinder as a Function of Pressure. These Plots Compare the Model 5 Results to those Obtained from the Shell Models Reported in [2] (Models 1 and 2).

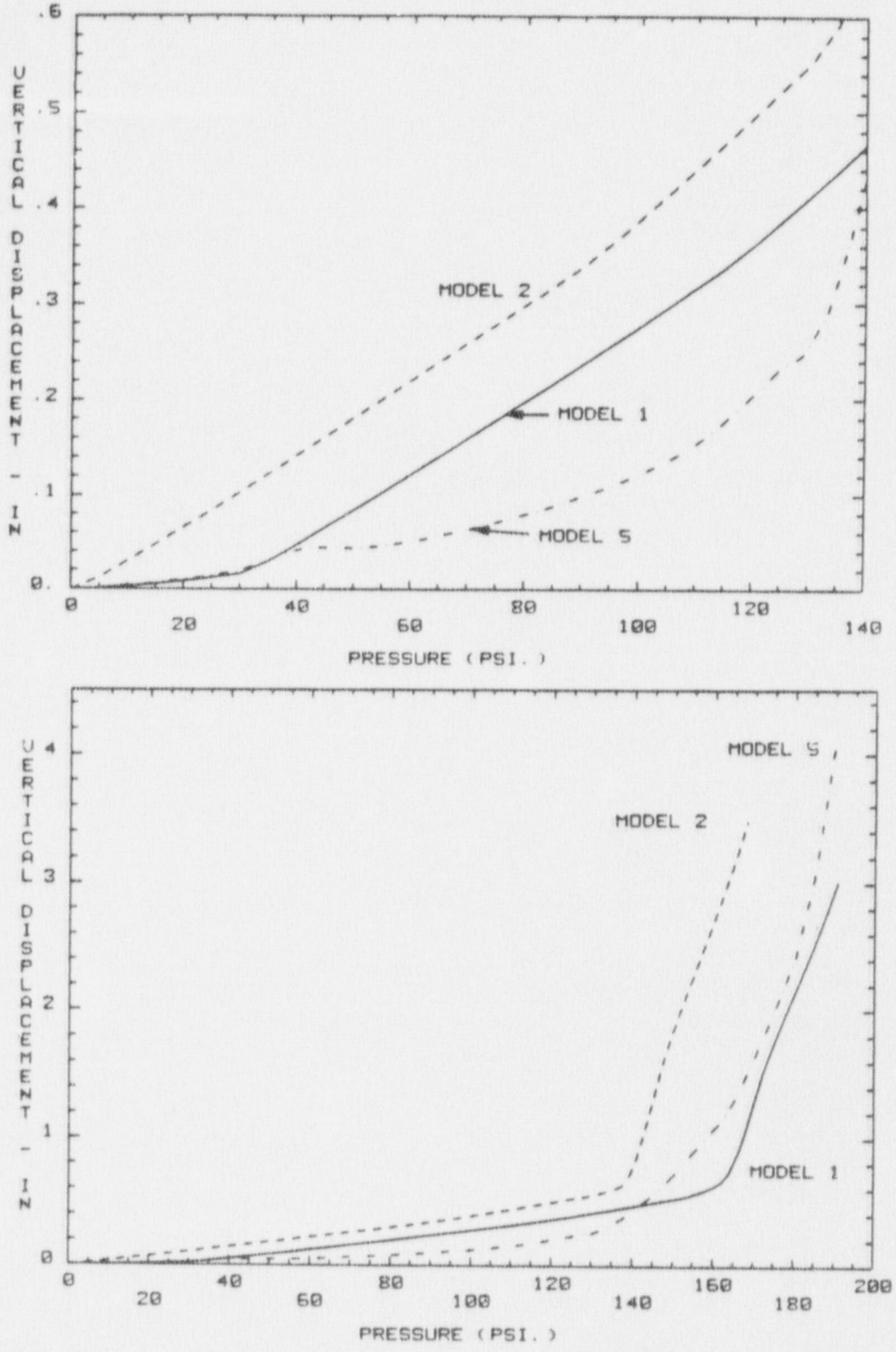

Figure 13. Vertical Displacement of the Dome Apex as a Function of Pressure. Results of the Shell Analysis with Cracking (Model 5) is compared to the Results of the Model 1 and Model 2 Analyses Reported in [2].

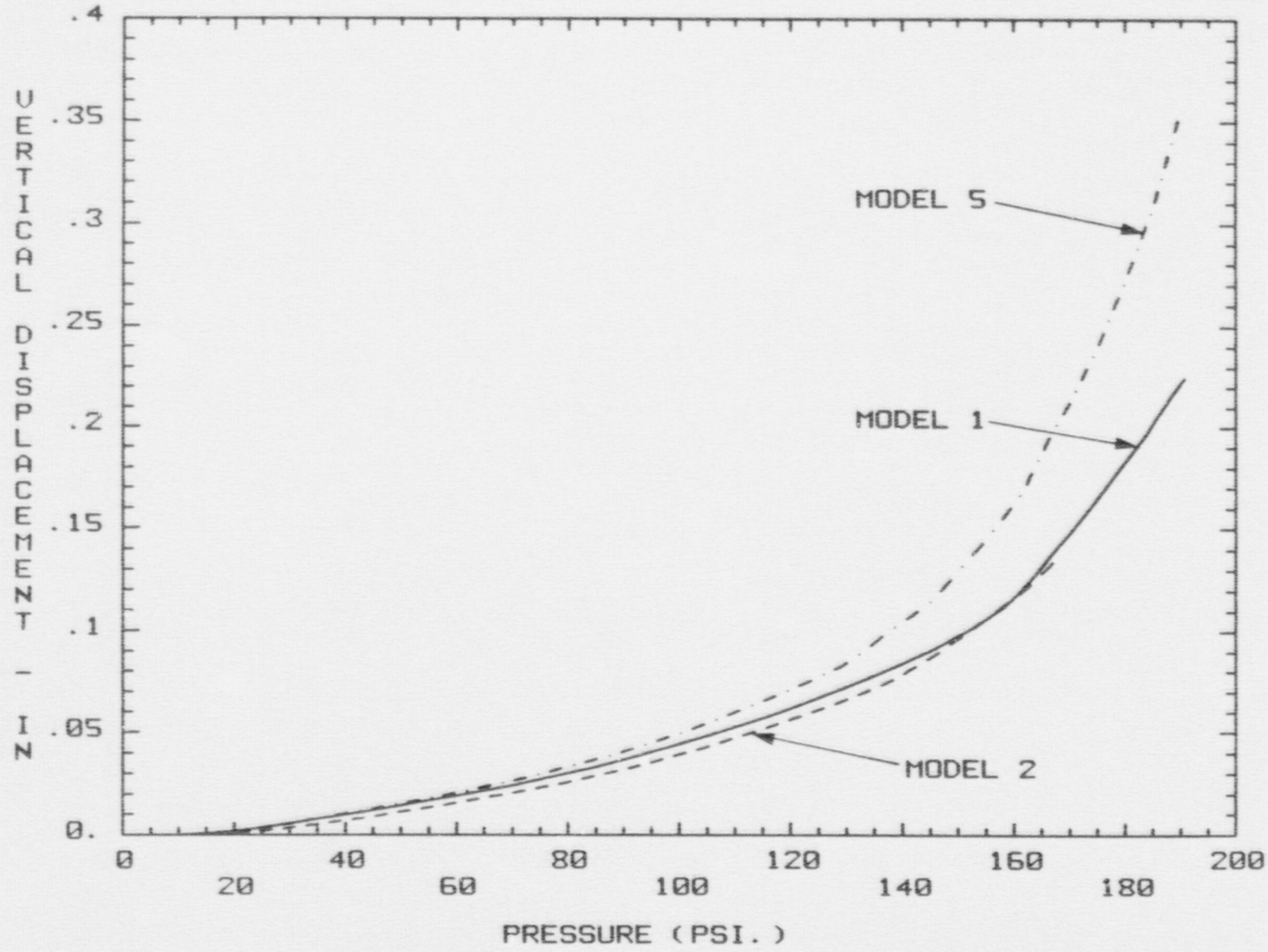

Figure 14. Vertical Displacement of the Basemat Beneath the Cylinder Wall Plotted as a Function of Pressure. The Results from Model 5 are Compared to the Results from Models 1 and 2 reported in [2].

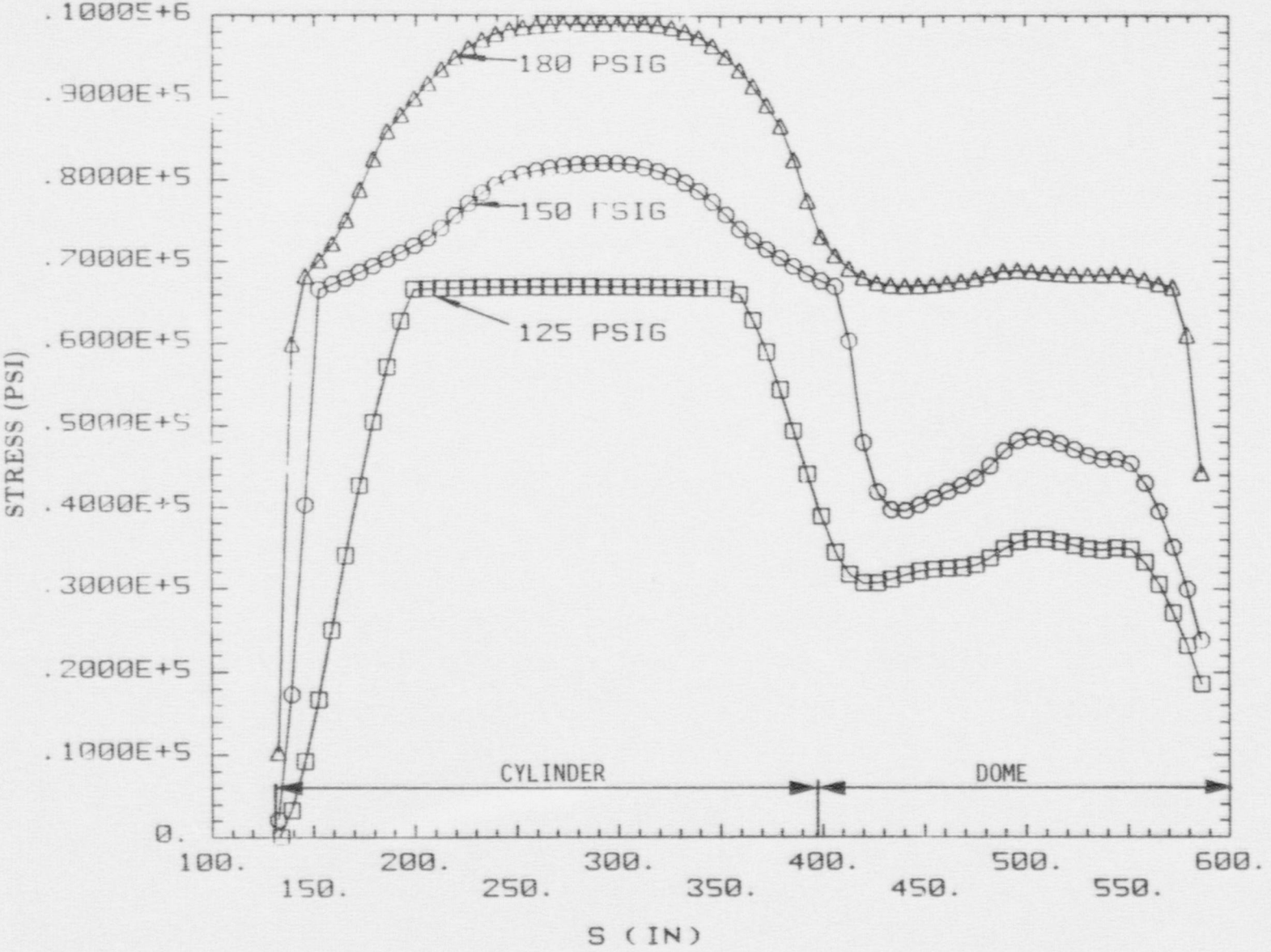

Figure 15. Stress in the Layer 1 Hoop Reinforcement as a Function of Position. (Model 5 Results)

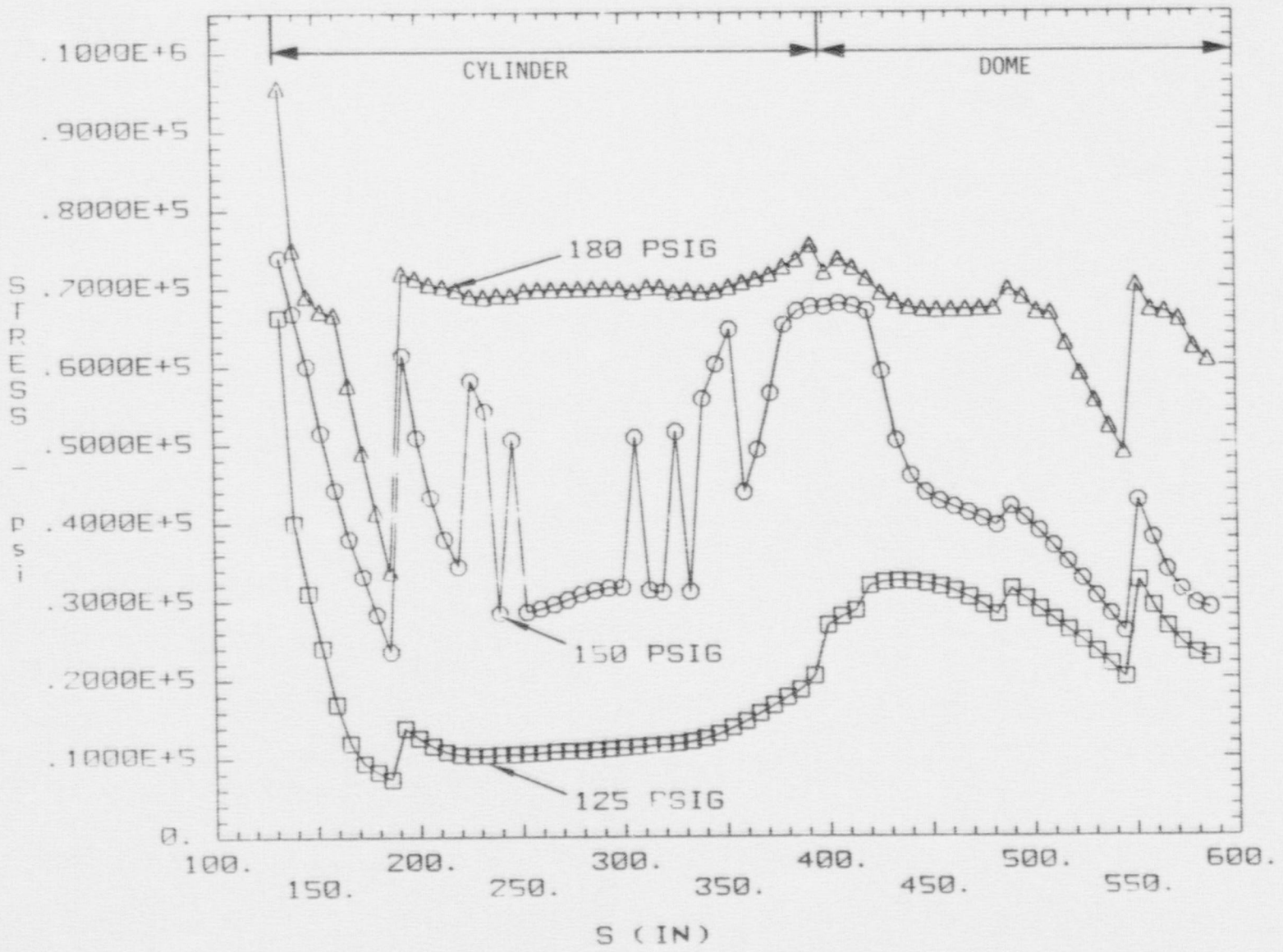

Figure 16. Stress in the Layer 2 Meridional Reinforcement as a Function of Position. (Model 5 Results)

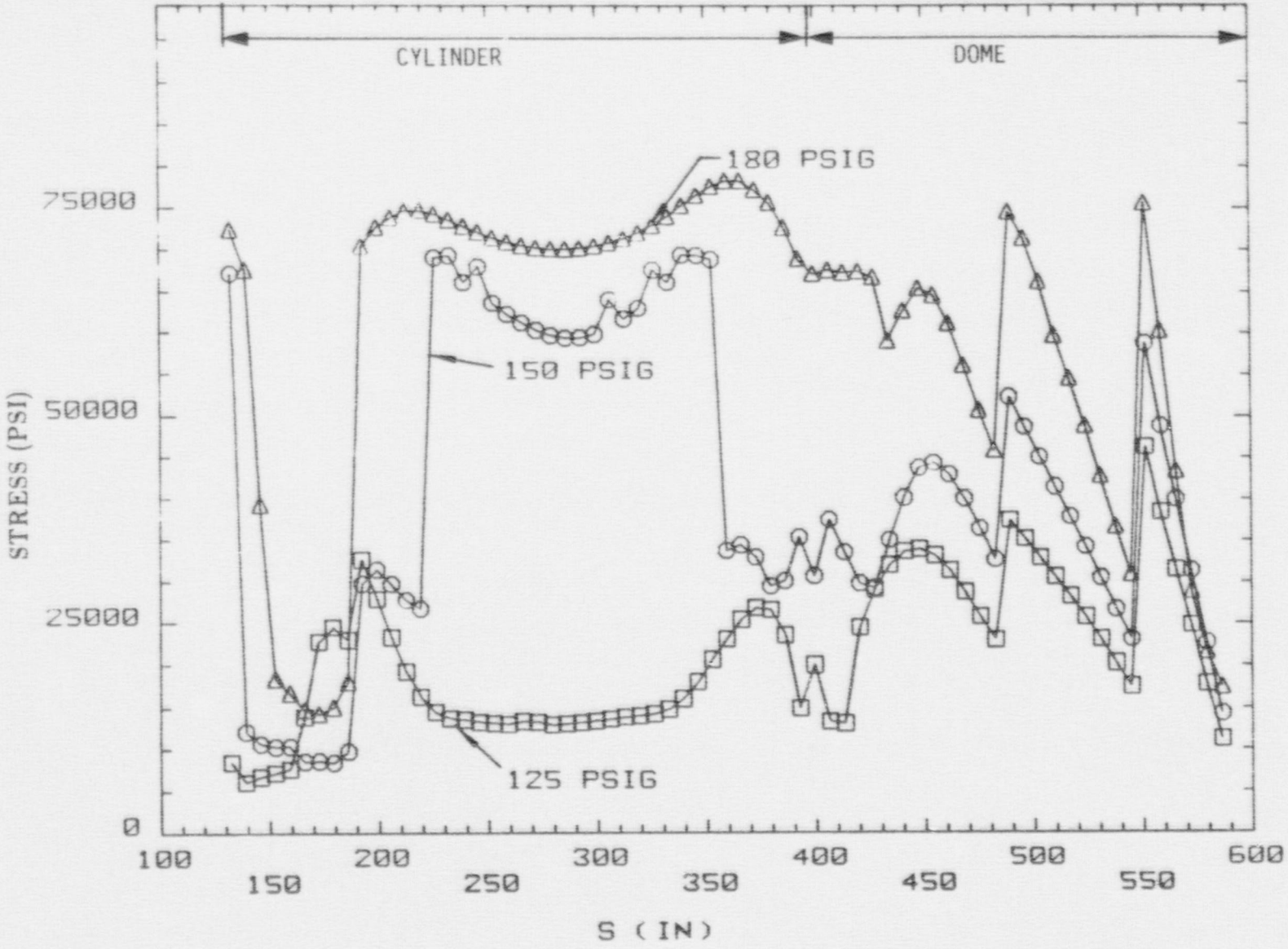

Figure 17. Stress in the Layer 5 Meridional Reinforcement as a Function of Position. (Model 5 Results).

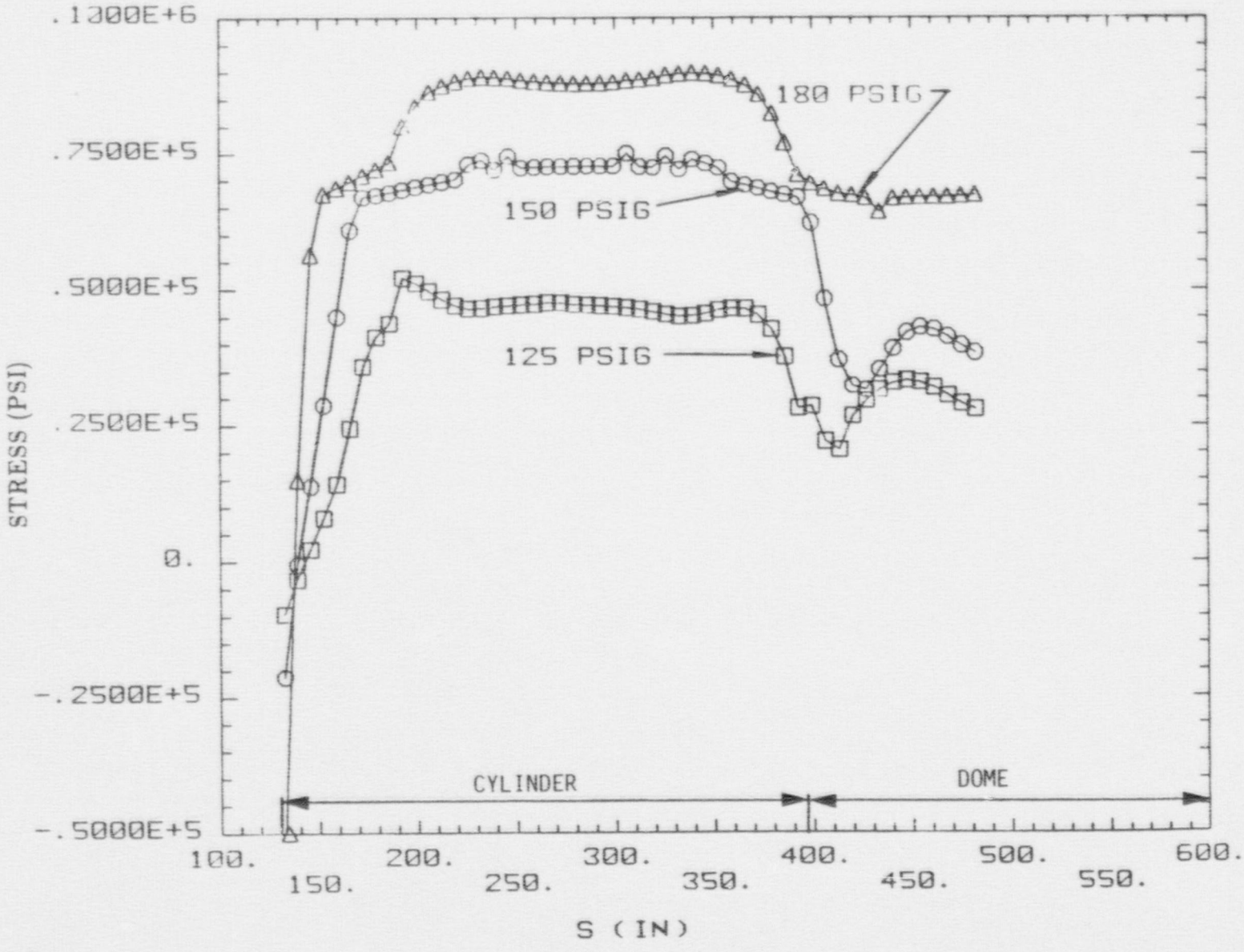

Figure 18. Stress in the Layer 8 Seismic Reinforcement as a Function of Position. (Model 5 Results)

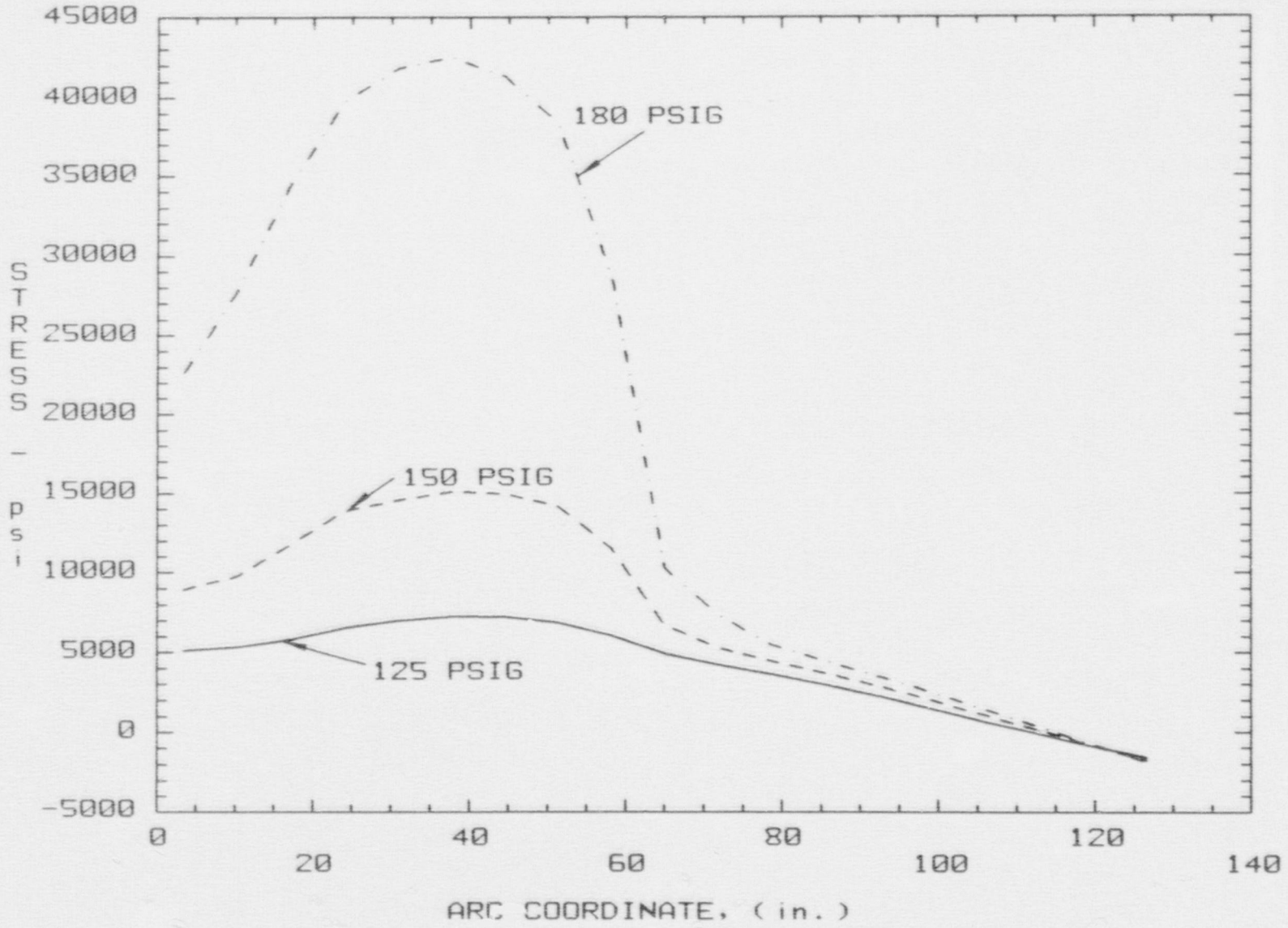

Figure 19. Meridional Stresses in the Bottom Rectangular Reinforcement in the Basemat. (Model 5 Results)

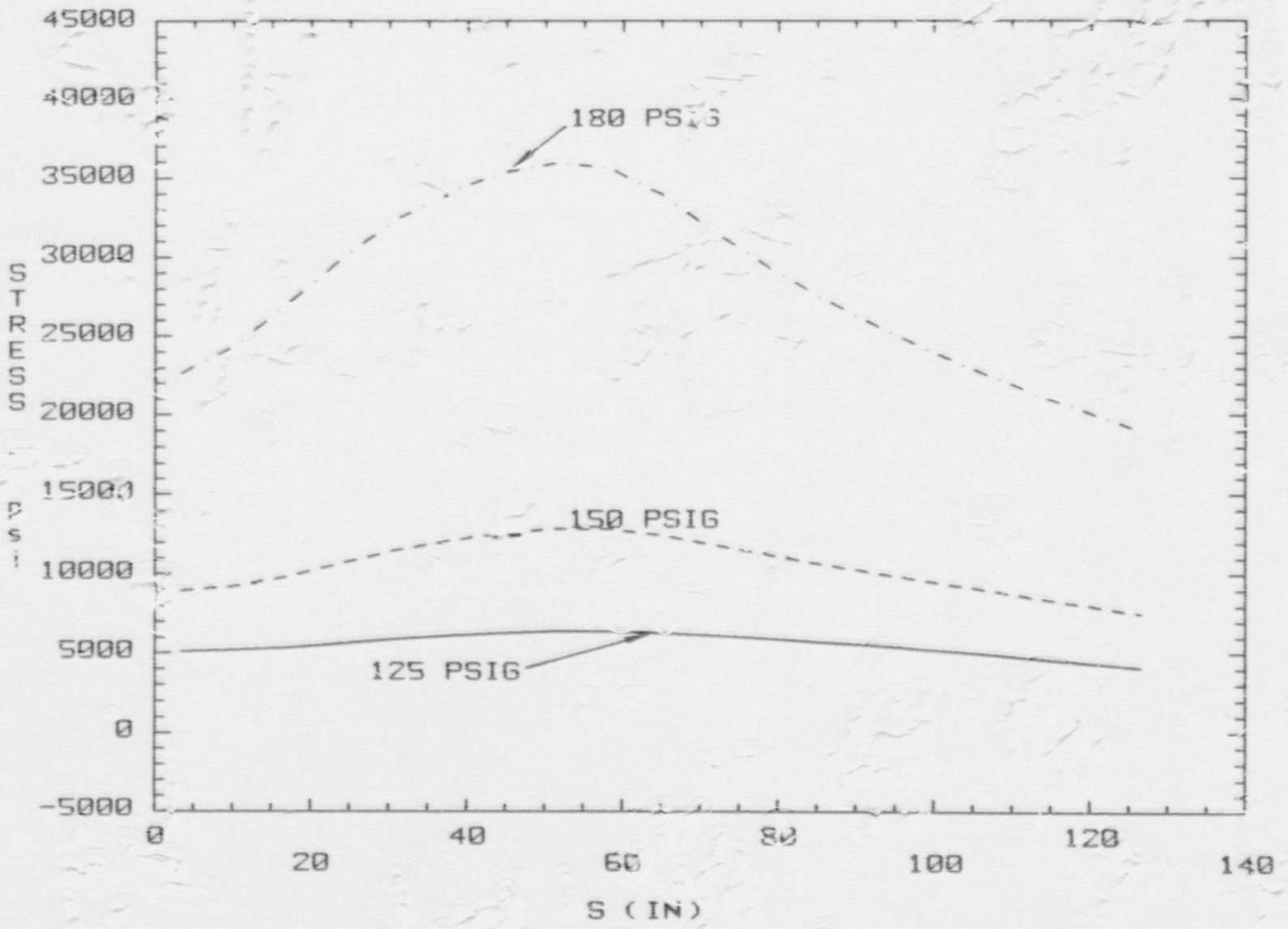

Figure 20. Hoop Stresses in the Bottom Rectangular Reinforcement in the Basemat. (Model 5 Results)

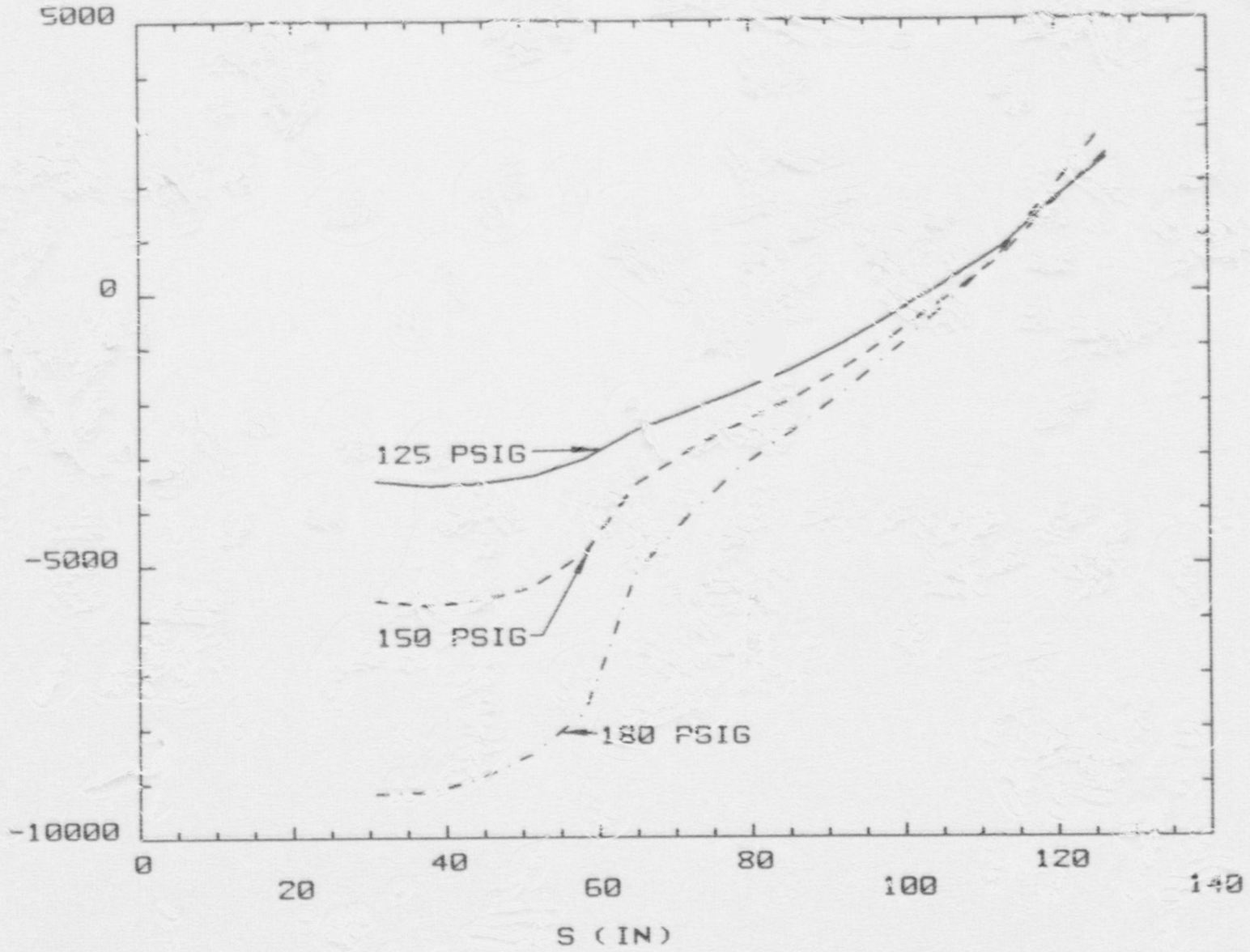

Figure 21. Stress in the Top Radial Reinforcement in the Basemat. (Model 5 Results)

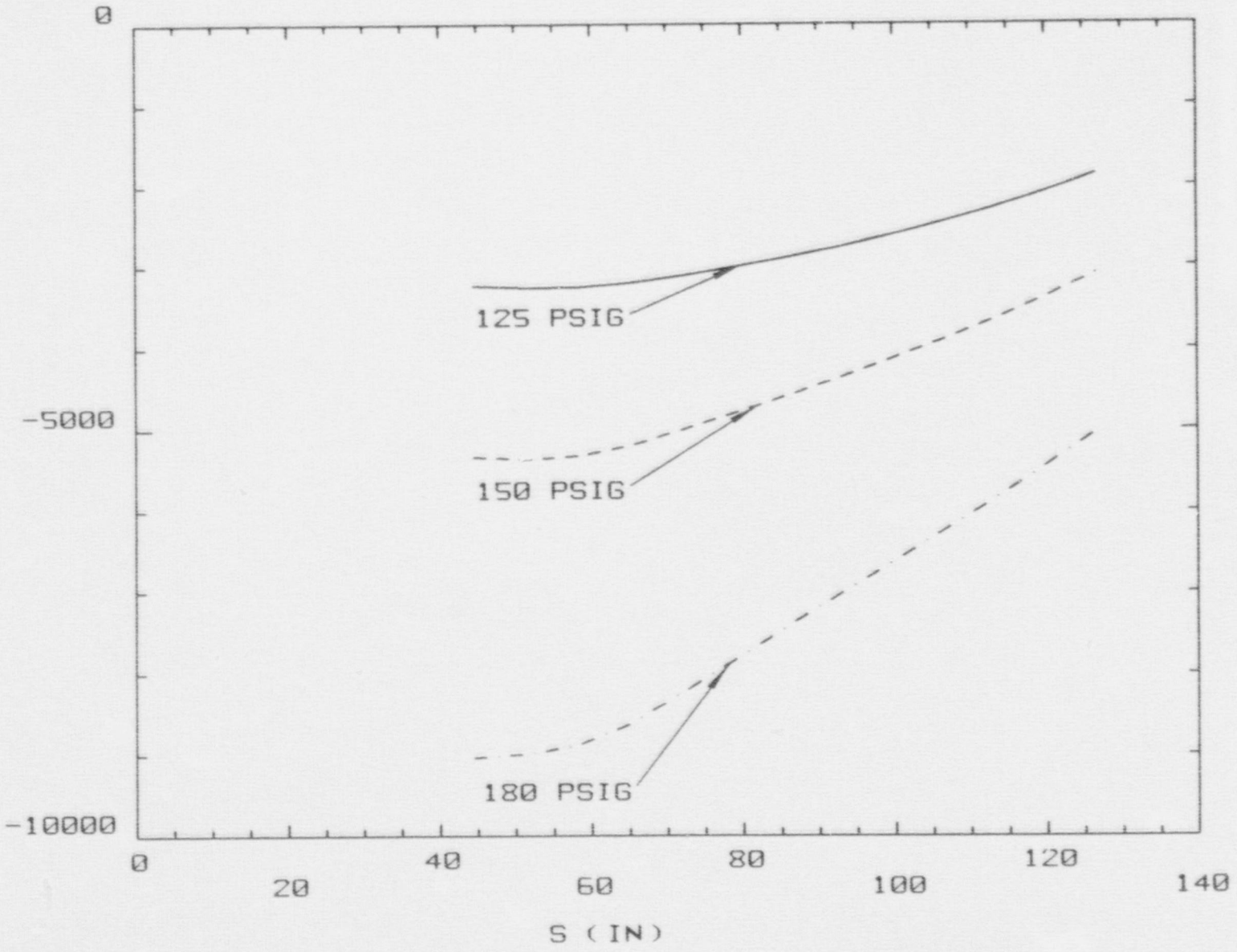

Figure 22. Stress in the Top Circumferential Reinforcement in the Basemat. (Model 5 Results)

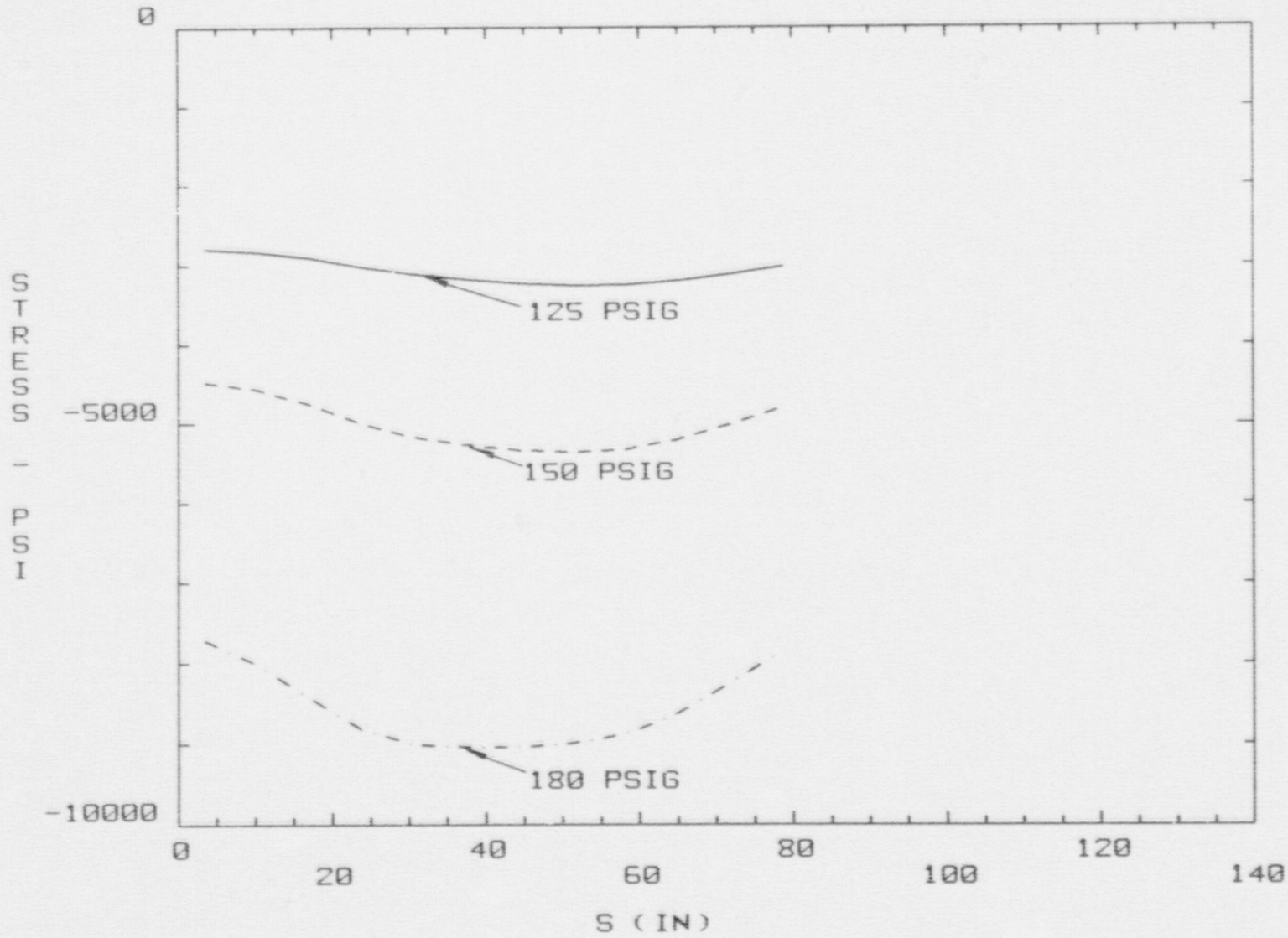

Figure 23. Hoop Stress in the Top Rectangular Reinforcement in the Basemat. (Model 5 Results)

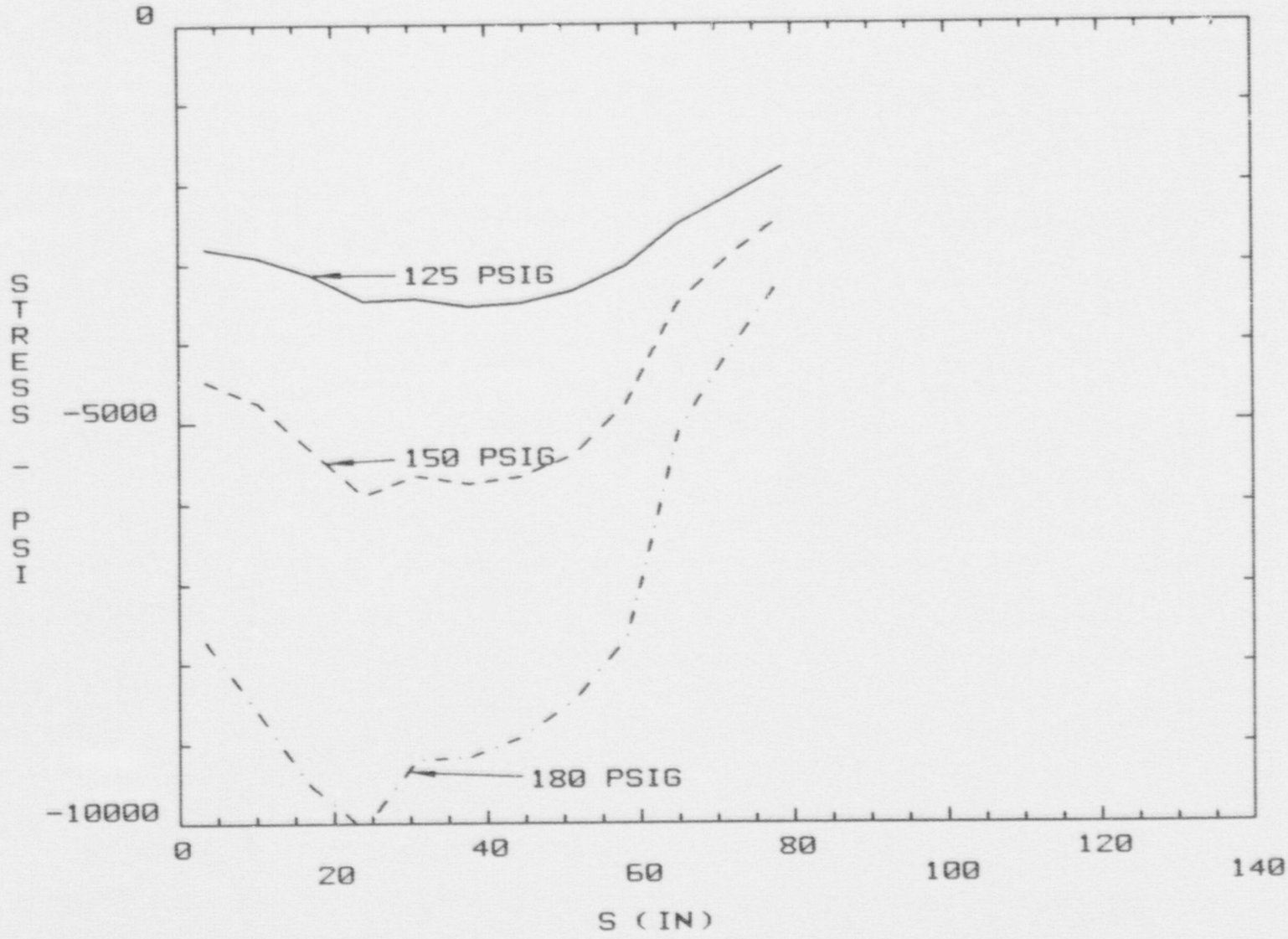

Figure 24. Meridional Stresses in the Top Rectangular Reinforcement in the Basemat. (Model 5 Results)

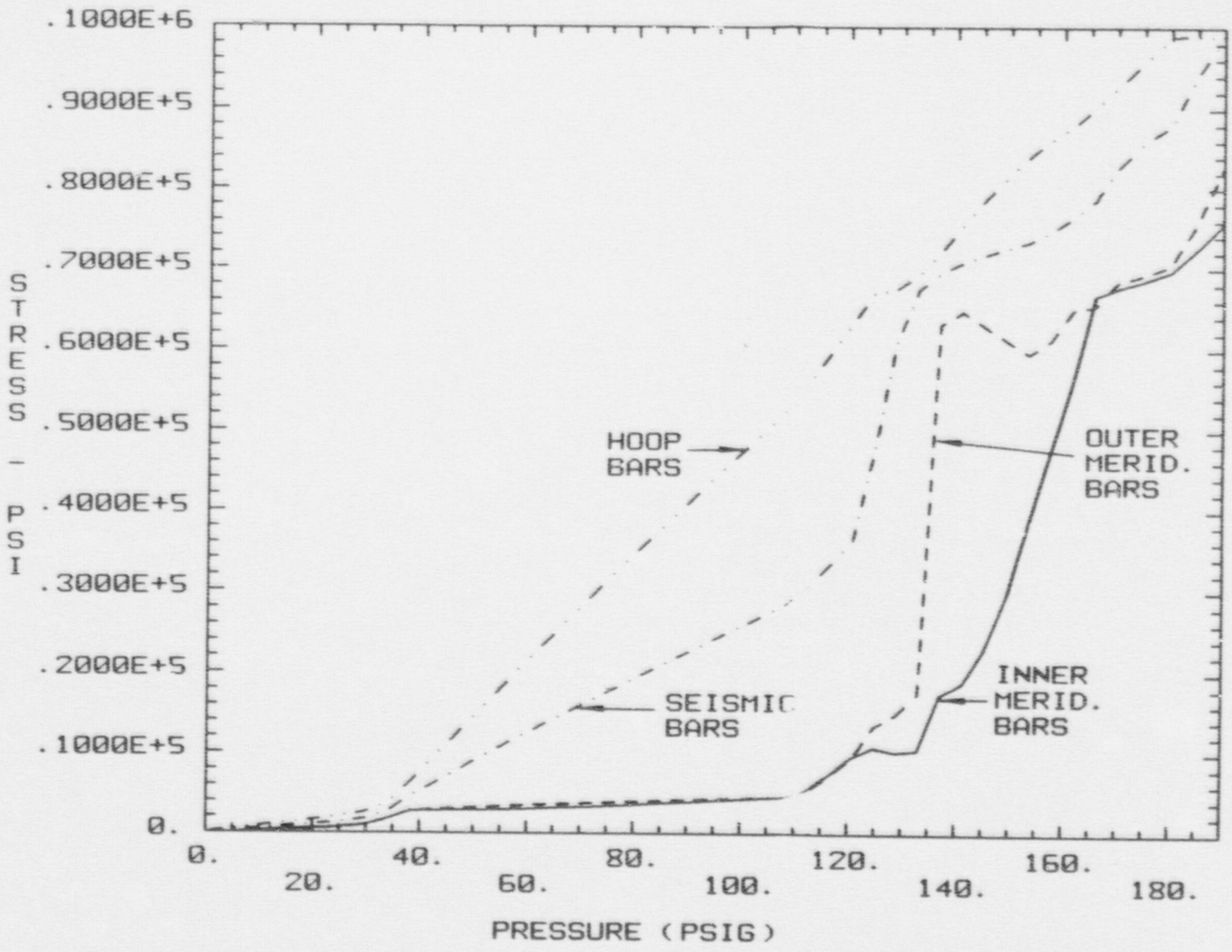

FIGURE 25. Stress in the Hoop, Meridional, and Seismic Bars at the Cylinder Midsection as a Function of Pressure. (Model 5 Results)

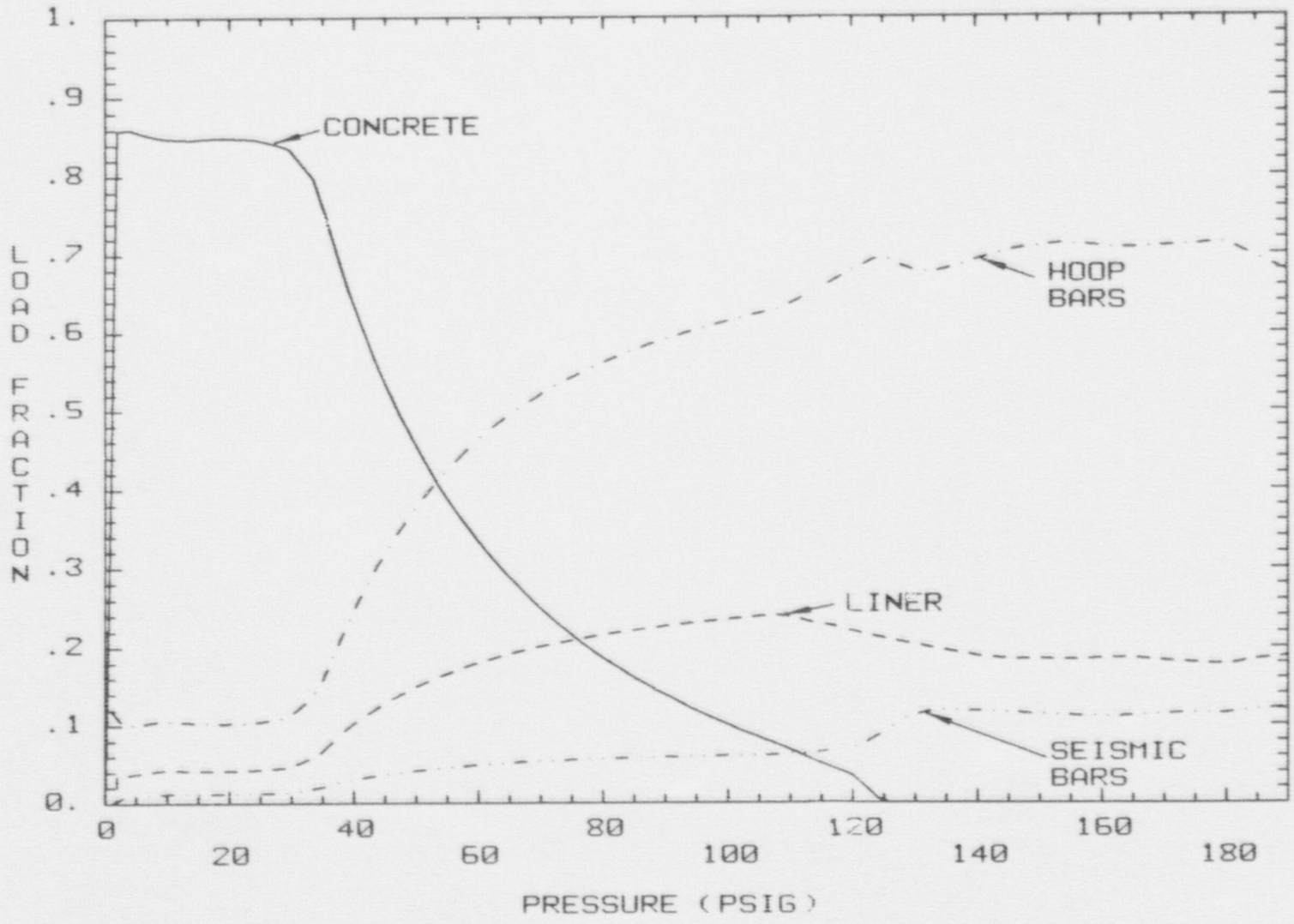

Figure 26. Fraction of the Total Hoop Membrane Load at the Cylinder Midheight Carried by the Concrete, Hoop Bars, Seismic Bars, and Liner. (Model 5 Results)

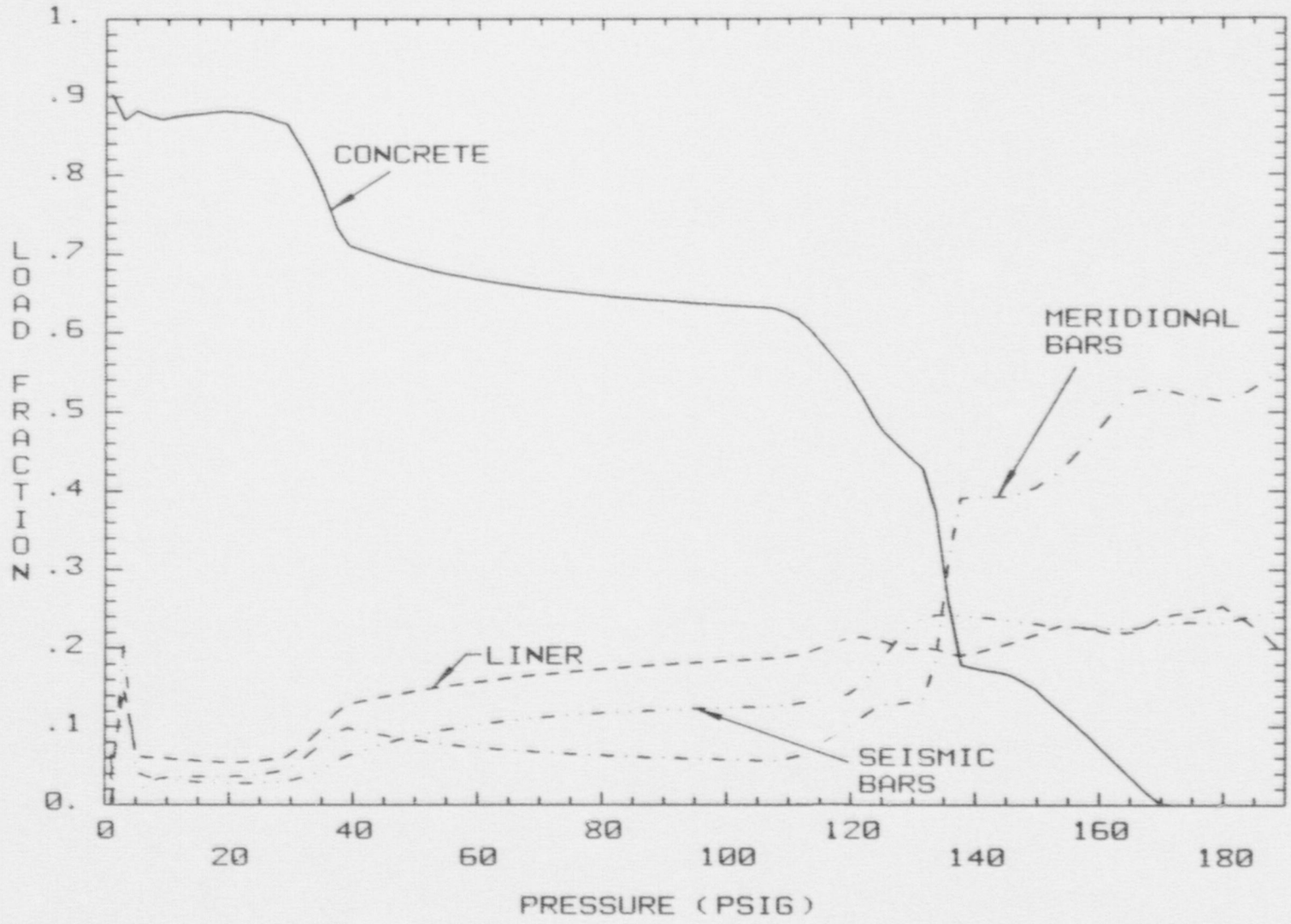

Figure 27. Fraction of the Total Meridional Membrane Load at the Cylinder Midheight Carried by the Concrete, Meridional Bars, Seismic Bars, and Liner. (Model 5 Results)

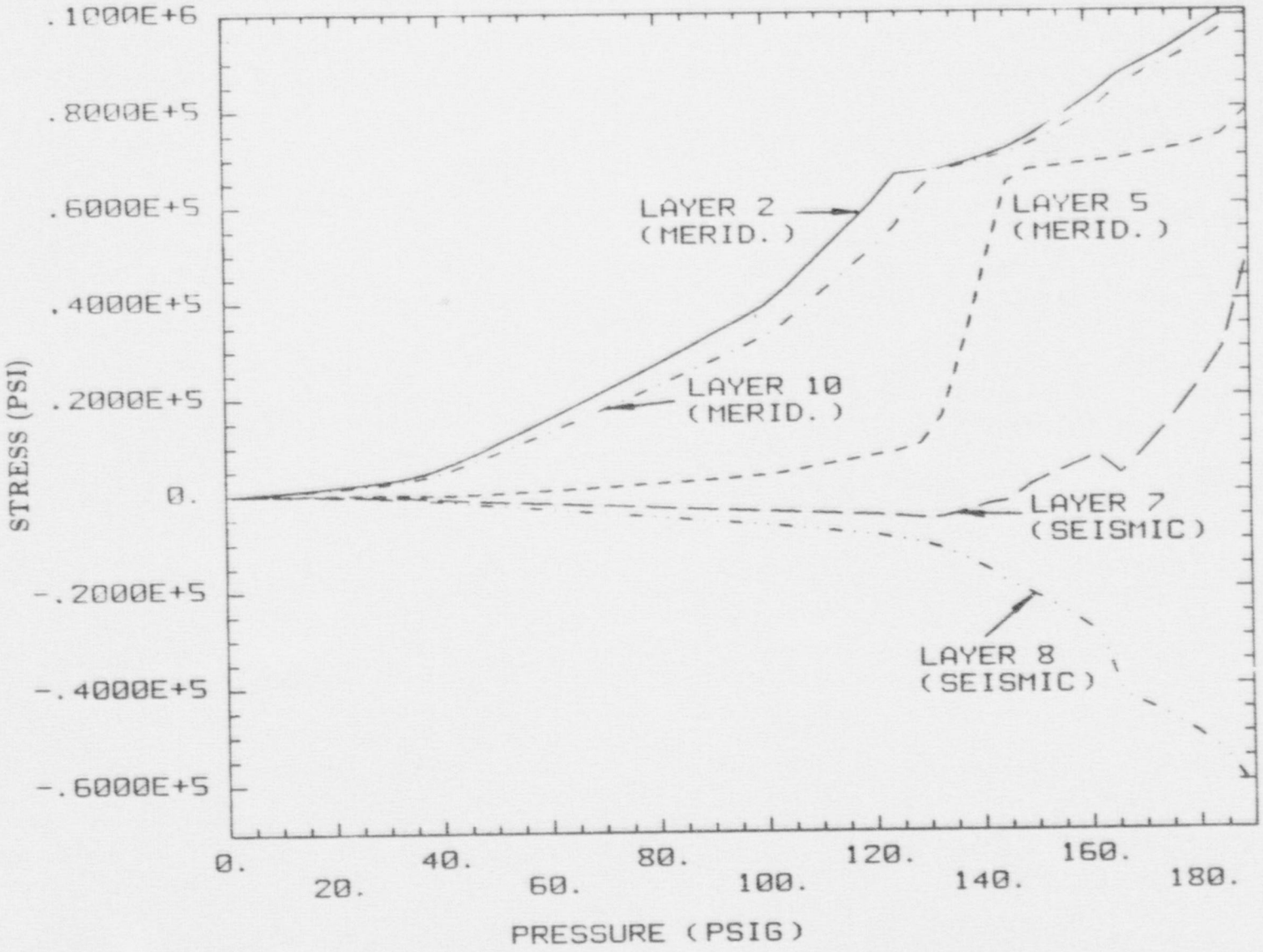

Figure 28. Stresses in the Meridional and Seismic Reinforcement at the Base of the Cylinder Plotted as a Function of Internal Pressure. (Model 5 Results)

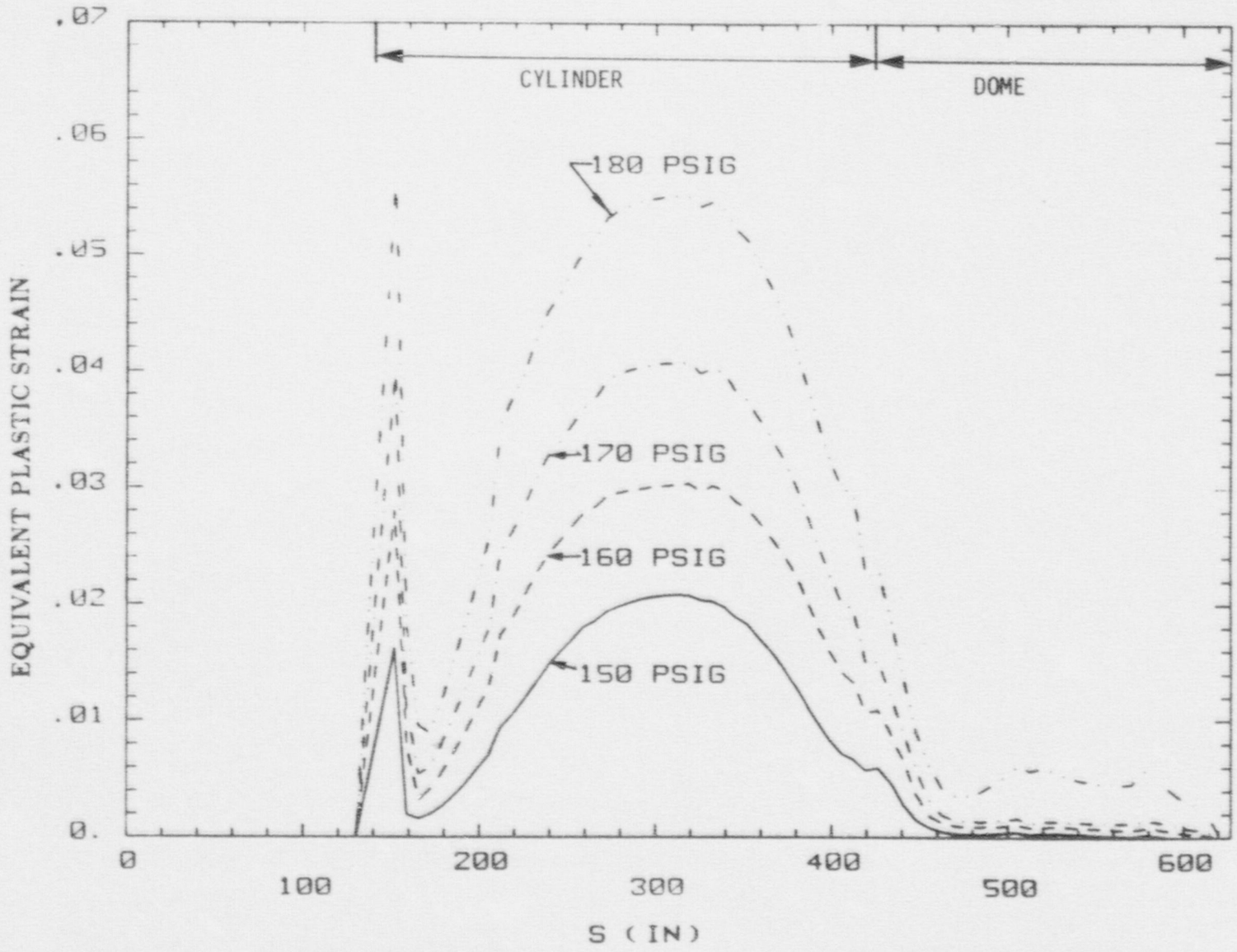

Figure 29. Equivalent Plastic Strain in the Liner as a Function of Position. (Model 5 Results)

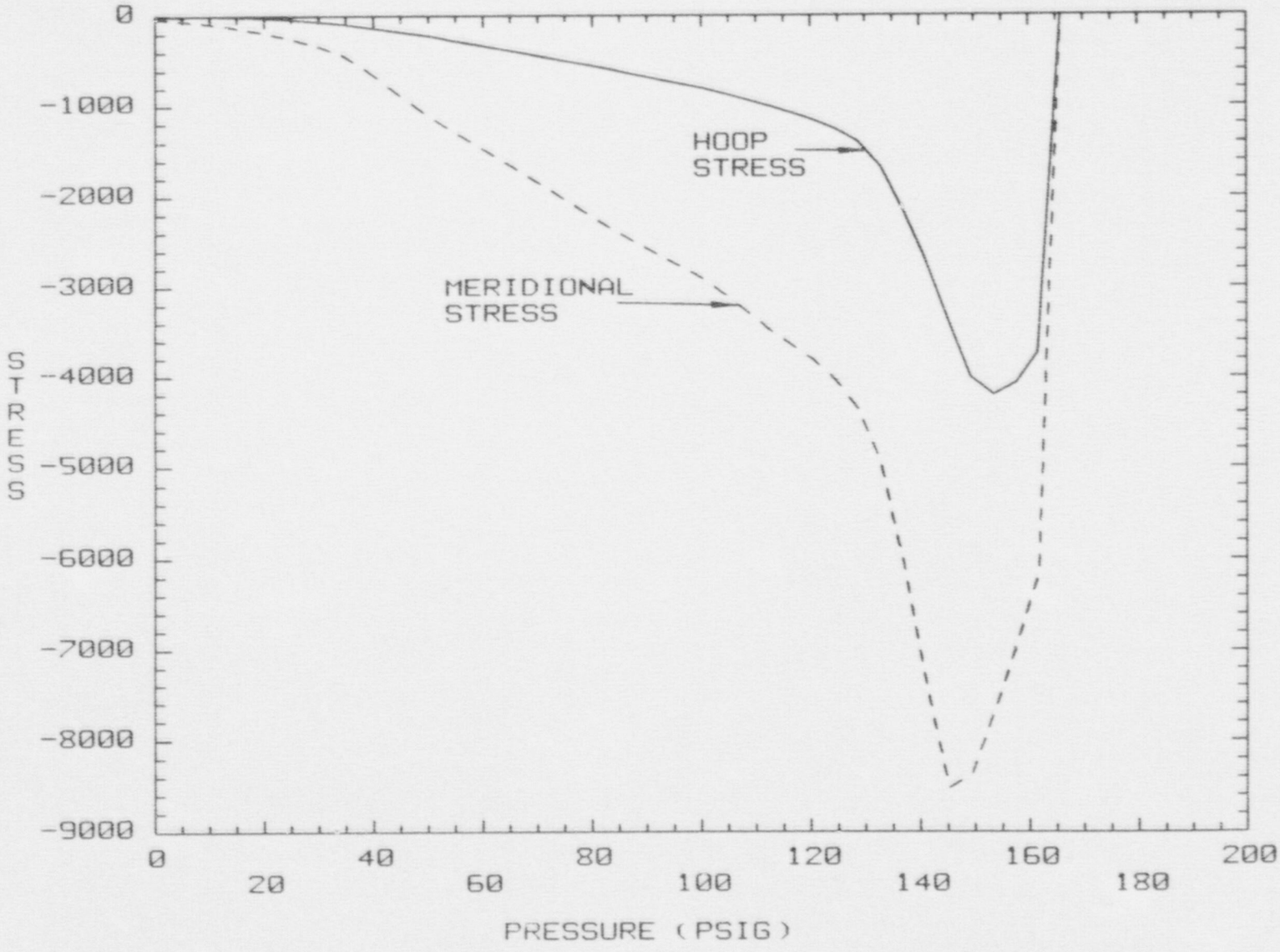

Figure 30. Hoop and Meridional Stresses Plotted as a Function of Internal Pressure for the Concrete on the Outer Cylinder Surface, 3 in. Above the Basemat. (Model 5 Results)

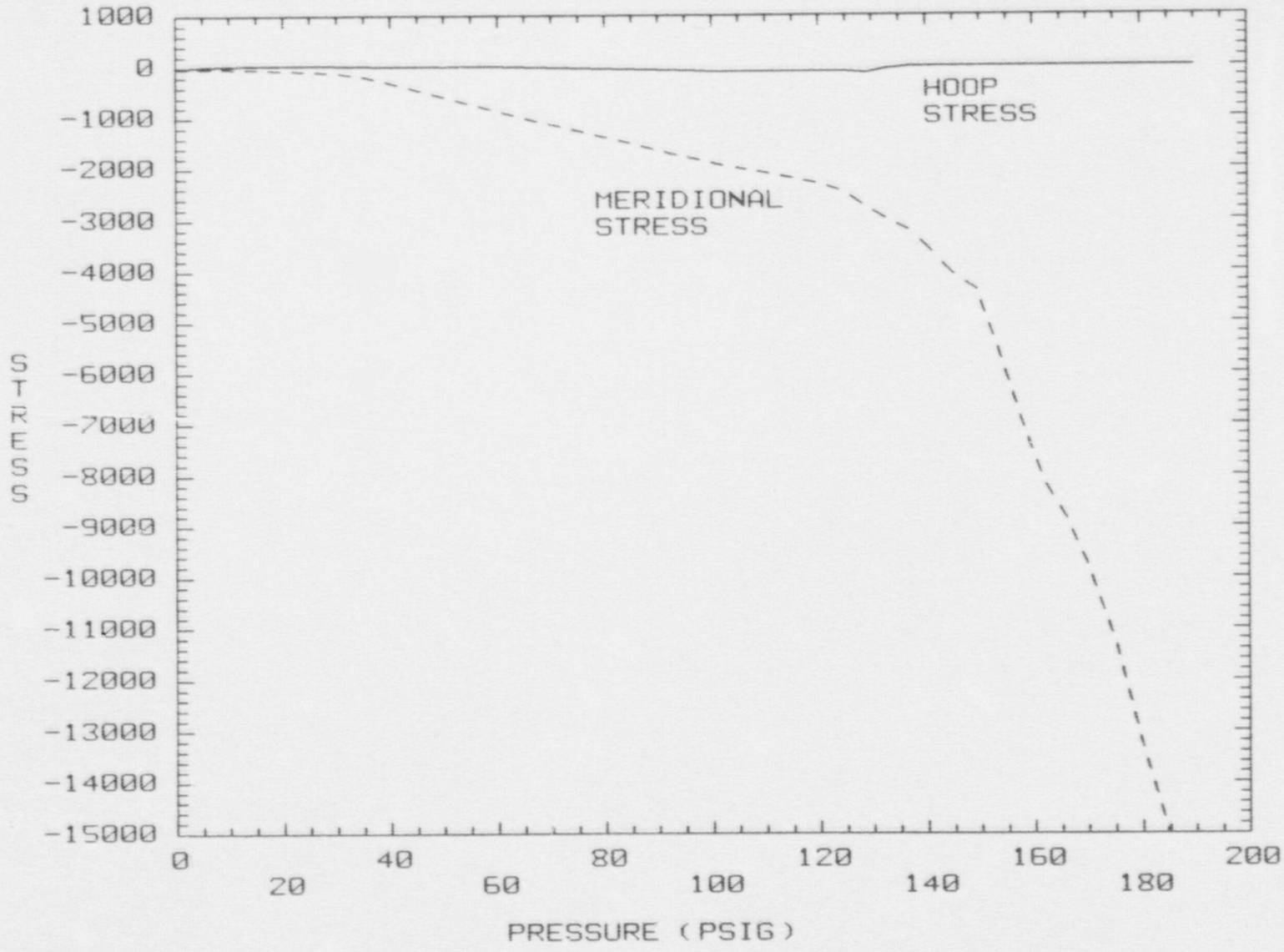

Figure 31. Hoop and Meridional Stresses Plotted as a Function of Internal Pressure for the Concrete on the Outer Cylinder Surface, 10 in. Above the Basemat. (Model 5 Results)

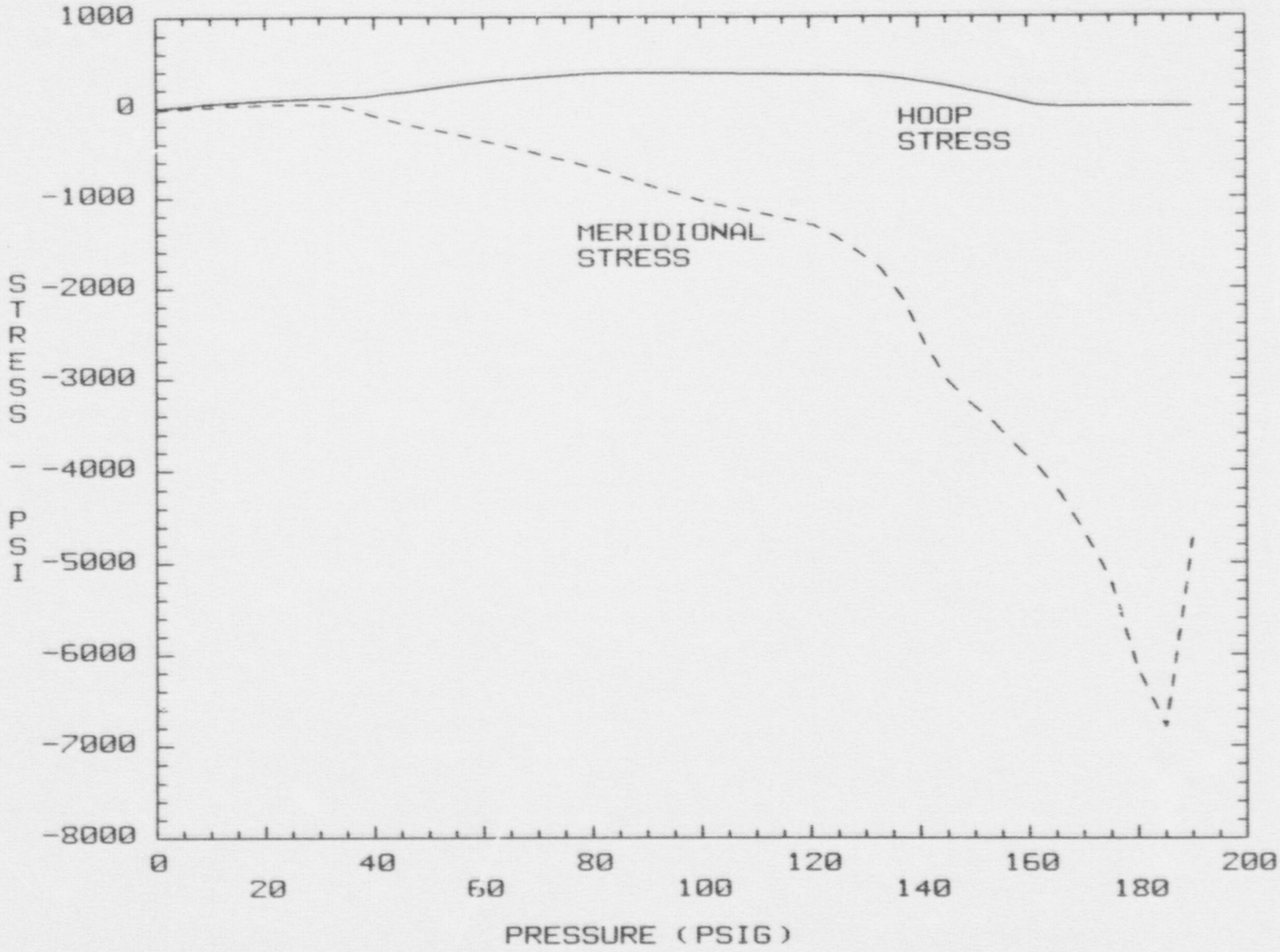

Figure 32. Hoop and Meridional Stresses Plotted as a Function of Internal Pressure for the Concrete on the Outer Cylinder Surface, 17 in. Above the Basemat. (Model 5 Results)

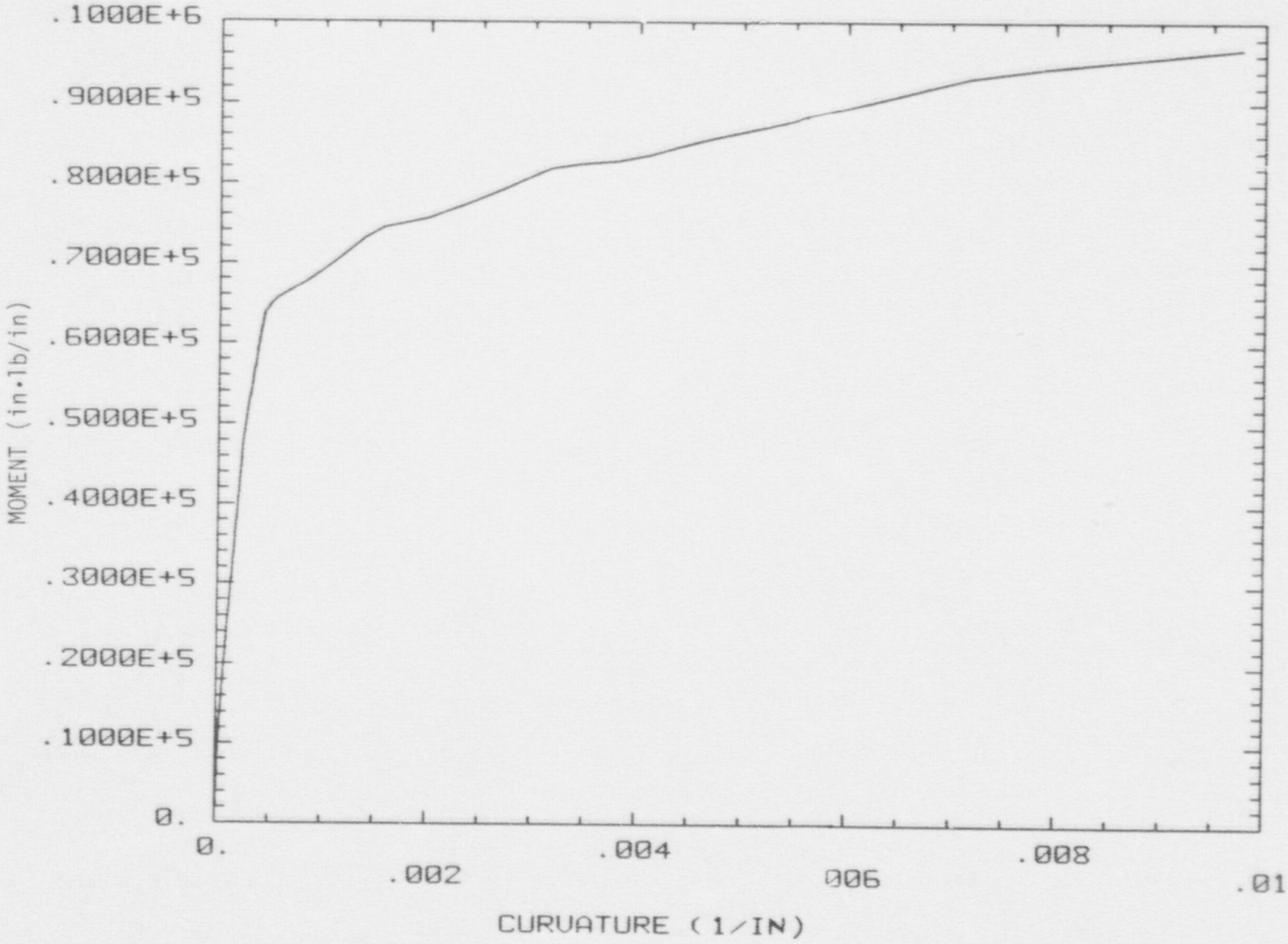

Figure 33. Moment-Curvature Relationship of the Base of the Cylinder. (Model 5 Results)

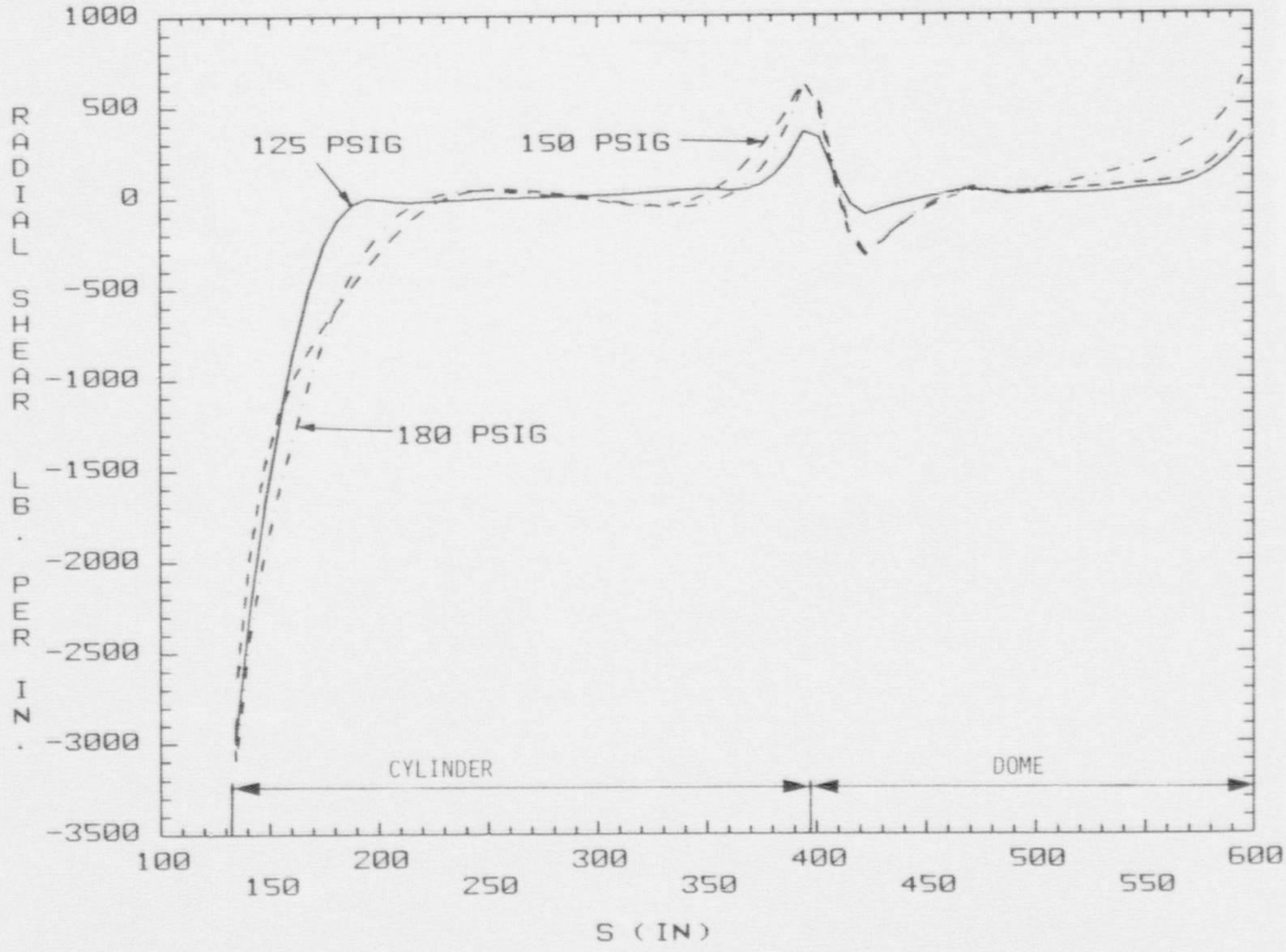

Figure 34. Radial Shear Force as a Function of Position in the Cylinder and Dome Regions. (Model 5 Results)

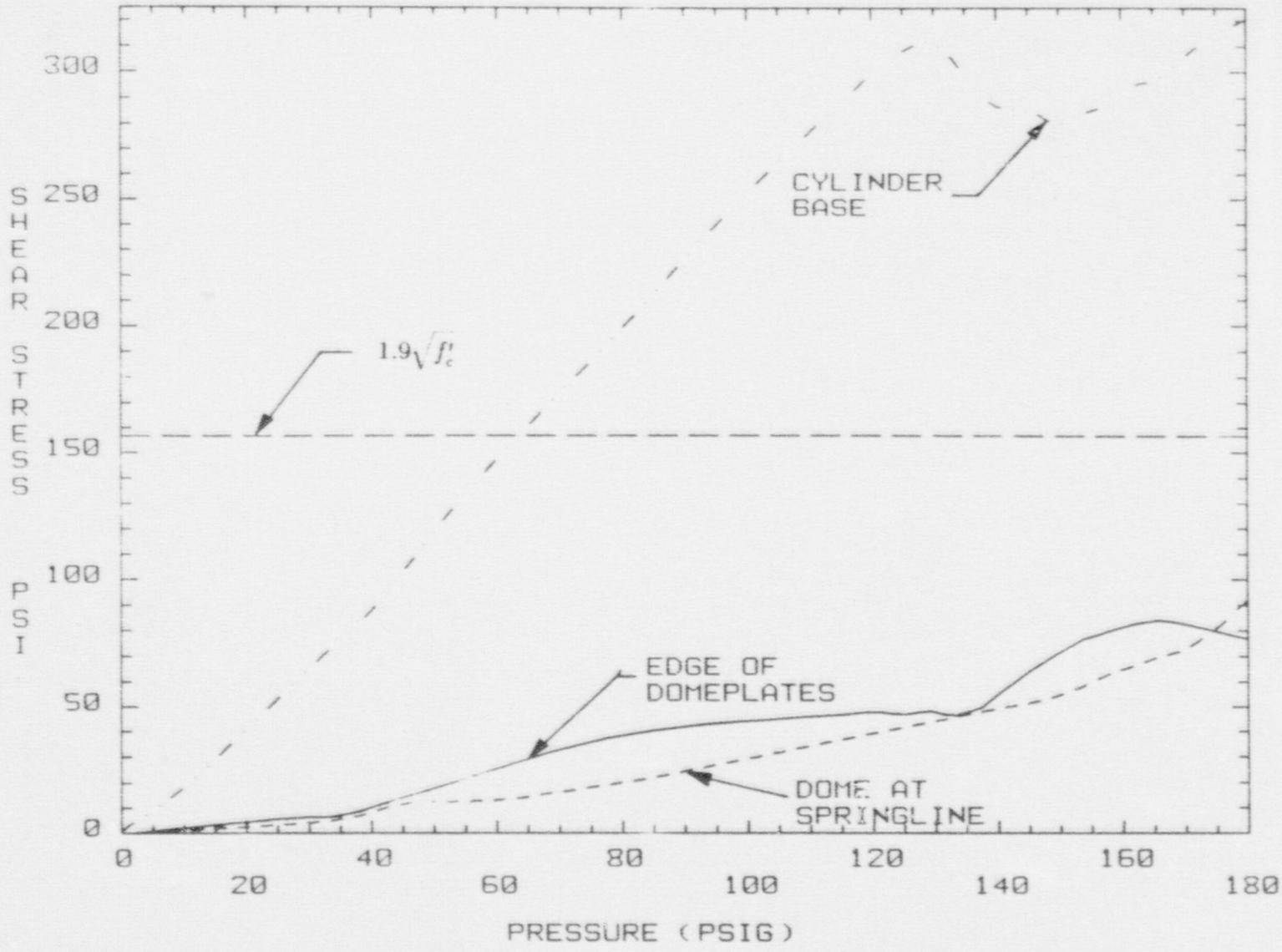

Figure 35. Radial Shear Stress as a Function of Pressure at Three Locations. (Model 5 Results)

APPENDIX A
LISTING OF MEMBRANE ANALYSIS PROGRAM

```
      COMMON STRESS(10), STRAIN(10), NPTS
      COMMON /OLD/ EPSHO,EPSVO,SHLO,SVLO,EPLO
      COMMON /LINER/ E,ET,ENU,D11,D12,YIELD
      DIMENSION STIFF(2,2), PSI(2), SINV(2,2)
      DATA NPTS/8/
      DATA STRESS/0.,66.6E3,73.3E3,85.6E3,99.E3,0.,0.,0.,
     *            0.,0./
      DATA STRAIN/0.,2.15E-3,1.18E-2,2.27E-2,4.61E-2,0.,0.,
     *            0.,0.,0./
      DATA E/30.E6/,ET/.256E6/,ENU/.3/,YIELD/50.2E3/,TL/.0625/
      DATA NH/4/,NV/2/,ND/2/
      DATA SH/.2222/,SV/.2222/,SD/.16/
      DATA R/136.875/,ABAR/.2/,PI/3.14159/,TOL/.00001/,W/1.6E5/
      OPEN(7, FILE='RDISP.NEU',STATUS='UNKNOWN')
      OPEN(8, FILE='HOOP.NEU' ,STATUS='UNKNOWN')
      OPEN(9, FILE='VERT.NEU' ,STATUS='UNKNOWN')
      OPEN(10,FILE='DIAG.NEU' ,STATUS='UNKNOWN')
      OPEN(11,FILE='LVM.NEU',STATUS='UNKNOWN')
      OPEN(12,FILE='LHOOP',STATUS='UNKNOWN')
      OPEN(13,FILE='LMERID',STATUS='UNKNOWN')
      OPEN(14,FILE='EPLH.NEU',STATUS='UNKNOWN')
      OPEN(15,FILE='EPLV.NEU',STATUS='UNKNOWN')
      OPEN(16,FILE='EPLZ.NEU',STATUS='UNKNOWN')
      OPEN(17,FILE='EPLO.NEU',STATUS='UNKNOWN')
      WRITE(7,'(''BEGIN CURVE,MDISPR'')')
      WRITE(7,'(''1,RADIAL DISPLACEMENT, MEMBRANE THEORY'')')
      WRITE(7,'(''PRESSURE, PSI.'')')
      WRITE(7,'(''R-DISP. - IN.'')')
      WRITE(7,'(''0.,200.,0.,12.,93'')')
      WRITE(7,'(''NOLOG,MONO'')')
C
      WRITE(14,'(''BEGIN CURVE,EPLH'')')
      WRITE(14,'(''1,HORIZONTAL PLASTIC STRAIN - MEMBRANE THEORY'')')
      WRITE(14,'(''PRESSURE, PSI.'')')
      WRITE(14,'(''STRAIN'')')
      WRITE(14,'(''0.,200.,0.,1.,93'')')
      WRITE(14,'(''NOLOG,MONO'')')
C
```

```
      WRITE(15,'(''BEGIN CURVE,EPLV'')')
      WRITE(15,'(''1,VERTICAL PLASTIC STRAIN - MEMBRANE THEORY'')')
      WRITE(15,'(''PRESSURE, PSI.'')')
      WRITE(15,'(''STRAIN'')')
      WRITE(15,'(''0.,200.,0.,1.,93'')')
      WRITE(15,'(''NOLOG,MONO'')')
C
      WRITE(16,'(''BEGIN CURVE,EPLZ'')')
      WRITE(16,'(''1,PLASTIC STRAIN,THICKNESS - MEMBRANE THEORY'')')
      WRITE(16,'(''PRESSURE, PSI.'')')
      WRITE(16,'(''STRAIN'')')
      WRITE(16,'(''0.,200.,0.,1.,93'')')
      WRITE(16,'(''NOLOG,MONO'')')
C
      WRITE(17,'(''BEGIN CURVE,EPL0'')')
      WRITE(17,'(''1,EQUIVALENT PLASTIC STRAIN - MEMBRANE THEORY'')')
      WRITE(17,'(''PRESSURE, PSI.'')')
      WRITE(17,'(''STRAIN'')')
      WRITE(17,'(''0.,200.,0.,1.,93'')')
      WRITE(17,'(''NOLOG,MONO'')')
C
      WRITE(8,'(''BEGIN CURVE,MHOOP'')')
      WRITE(8,'(''1,STRESS IN HOOP BARS, MEMBRANE THEORY'')')
      WRITE(8,'(''PRESSURE, PSI.'')')
      WRITE(8,'(''STRESS - PSI.'')')
      WRITE(8,'(''0.,200.,0.,99.E3,93'')')
      WRITE(8,'(''NOLOG,MONO'')')
C
      WRITE(9,'(''BEGIN CURVE,MVERT'')')
      WRITE(9,'(''1,STRESS IN VERTICAL BARS, MEMBRANE THEORY'')')
      WRITE(9,'(''PRESSURE, PSI.'')')
      WRITE(9,'(''STRESS - PSI.'')')
      WRITE(9,'(''0.,200.,0.,99.E3,93'')')
      WRITE(9,'(''NOLOG,MONO'')')
C
      WRITE(10,'(''BEGIN CURVE,MDIAG'')')
      WRITE(10,'(''1,STRESS IN DIAGONAL BARS, MEMBRANE THEORY'')')
      WRITE(10,'(''PRESSURE, PSI.'')')
      WRITE(10,'(''STRESS - PSI.'')')
      WRITE(10,'(''0.,200.,0.,99.E3,93'')')
      WRITE(10,'(''NOLOG,MONO'')')
```

```
C
      WRITE(11,'(''BEGIN CURVE,MLINR'')')
      WRITE(11,'(''1,VON MISES STRESS IN LINER, MEMBRANE THEORY'')')
      WRITE(11,'(''PRESSURE, PSI.'')')
      WRITE(11,'(''STRESS - PSI.'')')
      WRITE(11,'(''0.,200.,0.,99.E3,93'')')
      WRITE(11,'(''NOLOG,MONO'')')
C
      WRITE(12,'(''"LINER HOOP"'')')
      WRITE(13,'(''"LINER MERIDIONAL"'')')
      P = W / (PI * R * R)+1.
      RHI = 0.
      RVI = 0.
      EPSH = 0.
      EPSD = 0.
      EPSV = 0.
      D11 = E / (1. - ENU**2)
      D12 = ENU * D11
      DP = 2.
      DO 30 WHILE (P .LT. 210.)
      P = P + DP
C
C     Calculate applied stress resultants
C
      RHE = P * R / ABAR
      RVE = (P * R - W / (PI * R)) / (2. * ABAR)
 20   CONTINUE
C
C     Compute the tangent stiffness matrix
C
      STIFF(1,1) = NH * SH * TMOD(EPSH) + .25 * ND * SD * TMOD(EPSD) +
     *             TL * D11 / ABAR
      STIFF(1,2) = .25 * ND * SD * TMOD(EPSD) + TL * D12 / ABAR
      STIFF(2,1) = STIFF(1,2)
      STIFF(2,2) = NV * SV * TMOD(EPSV) + .25 * ND * SD * TMOD(EPSD) +
     *             TL * D11 / ABAR
C
C     Invert the tangent stiffness matrix
C
      DET = STIFF(1,1) * STIFF(2,2) - STIFF(1,2)**2
      SINV(1,1) =  STIFF(2,2) / DET
```

```
      SINV(2,2) =  STIFF(1,1) / DET
      SINV(1,2) = -STIFF(1,2) / DET
      SINV(2,1) =  SINV(1,2)
C
C     Calculate residual and check for convergence
C
      PSI(1) = RHI - RHE
      PSI(2) = RVI - RVE
      RNORM = SQRT( (PSI(1)**2 + PSI(2)**2) / (RHE**2 + RVE**2) )
C      WRITE(*,2)P,EPSH,RNORM
 2    FORMAT( ' PRESSURE = ',E10.4,' HOOP STRAIN = ',E12.5,
     *        ' RESIDUAL NORM. = ',E12.5)
      IF (RNORM .LT. TOL)
     *   GO TO 10
C
C     Compute strain increments for current iteration
C
      DEPSH = -(SINV(1,1) * PSI(1) + SINV(1,2) * PSI(2))
      DEPSV = -(SINV(2,1) * PSI(1) + SINV(2,2) * PSI(2))
      EPSH = EPSH + DEPSH
      EPSV = EPSV + DEPSV
      EPSD = .5 * (EPSH + EPSV)
C
C     Calculate new internal stress resultants
C
      CALL LINER (SHL,SVL,EPSH,EPSV,DEPL,EPLH,EPLV,EPLZ)
      TOA = TL / ABAR
      RHI = NH * SH * SIG(EPSH) + .5 * ND * SD * SIG(EPSD) + TOA * SHL
      RVI = NV * SV * SIG(EPSV) + .5 * ND * SD * SIG(EPSD) + TOA * SVL
      GO TO 20
 10   CONTINUE
C
C     Update values for strains, stresses, and plastic strain.
C
      EPLO = EPLO + DEPL
      EPSHO = EPSH
      EPSVO = EPSV
      SHLO = SHL
      SVLO = SVL
C
C     Write stresses and radial displacement to data files.
```

```
C
      SVERT = SIG(EPSV)
      SHORZ = SIG(EPSH)
      SDIAG = SIG(EPSD)
      RDISP = R * EPSH
      SVML = SQRT( SHL * SHL - SHL * SVL + SVL * SVL )
      WRITE(*,'('' SHL = '',E12.5,'' SVL = '',E12.5,'' DEPL = '',E12.5,
     *'' SVML = '',E12.5)')SHL,SVL,DEPL,SVML
      WRITE(7,1) P,RDISP
      WRITE(8,1) P,SHORZ
      WRITE(9,1) P,SVERT
      WRITE(10,1) P,SDIAG
      WRITE(11,1) P,SVML
      WRITE(12,1) P,SHL
      WRITE(13,1) P,SVL
      WRITE(14,1) P,EPLH
      WRITE(15,1) P,EPLV
      WRITE(16,1) P,EPLZ
      WRITE(17,1) P,EPLO
1     FORMAT(E12.5,',',E12.5)
30    CONTINUE
      WRITE (7,'(''END CURVE,MDISPR'')')
      WRITE (8,'(''END CURVE,MHOOP'')')
      WRITE (9,'(''END CURVE,MVERT'')')
      WRITE (10,'(''END CURVE,MDIAG'')')
      WRITE (11,'(''END CURVE,MLINR'')')
      WRITE (12,'(''END CURVE,LHOOP'')')
      WRITE (13,'(''END CURVE,LMERID'')')
      WRITE (14,'(''END CURVE,EPLH'')')
      WRITE (15,'(''END CURVE,EPLV'')')
      WRITE (16,'(''END CURVE,EPLZ'')')
      WRITE (17,'(''END CURVE,EPLO'')')
      STOP
      END
C
      FUNCTION SIG(EPS)
      COMMON STRESS(10), STRAIN(10), NPTS
      CALL SEARCH (EPS,I1,I2)
      EPS1 = STRAIN(I1)
      EPS2 = STRAIN(I2)
      SIG1 = STRESS(I1)
```

```
      SIG2 = STRESS(I2)
      SIG = SIG1 + (SIG2 - SIG1) / (EPS2 - EPS1) * (EPS - EPS1)
      RETURN
      END
C
      FUNCTION TMOD(EPS)
      COMMON STRESS(10), STRAIN(10) ,NPTS
      CALL SEARCH (EPS,I1,I2)
      TMOD = (STRESS(I2) - STRESS(I1)) / (STRAIN(I2) - STRAIN(I1))
      RETURN
      END
C
      SUBROUTINE SEARCH (EPS,I1,I2)
      COMMON STRESS(10), STRAIN(10), NPTS
      DO 10 I = 1,NPTS
         IF (EPS .GE. STRAIN(I) .AND. EPS .LT. STRAIN(I+1)) THEN
           I1 = I
           I2 = I + 1
           GO TO 20
         END IF
10       CONTINUE
      WRITE (6,1)
1     FORMAT (' ERROR, MAXIMUM REBAR STRAIN EXCEEDED.')
      WRITE (7,'(''END CURVE,MDISPR'')')
      WRITE (8,'(''END CURVE,MHOOP'')')
      WRITE (9,'(''END CURVE,MVERT'')')
      WRITE (10,'(''END CURVE,MDIAG'')')
      WRITE (11,'(''END CURVE,MLINR'')')
      WRITE (12,'(''END CURVE,LHOOP'')')
      WRITE (13,'(''END CURVE,LMERID'')')
      WRITE (14,'(''END CURVE,EPLH'')')
      WRITE (15,'(''END CURVE,EPLV'')')
      WRITE (16,'(''END CURVE,EPLZ'')')
      WRITE (17,'(''END CURVE,EPLO'')')
      STOP
20    RETURN
      END
C
      SUBROUTINE LINER (SHL,SVL,EPSH,EPSV,DEPL,EPLH,EPLV,EPLZ)
      COMMON /OLD/ EPSHO,EPSVO,SHLO,SVLO,EPLO
      COMMON /LINER/ E,ET,ENU,D11,D12,YIELD
```

```
      H = (E * ET) / (E - ET)
C
C     Calculate strain increments
C
      DEPSH = EPSH - EPSHO
      DEPSV = EPSV - EPSVO
C
C     Compute trial stress increments
C
      DSHL = D11 * DEPSH + D12 * DEPSV
      DSVL = D12 * DEPSH + D11 * DEPSV
      DSIGKK = DSHL + DSVL
      SHLT = SHLO + DSHL
      SVLT = SVLO + DSVL
      SIGKK = SHLT + SVLT
C
C     Compute trial deviatoric stresses
C
      DEVHLT = SHLT - SIGKK / 3.
      DEVVLT = SVLT - SIGKK / 3.
C
C     Calculate norm of trial deviatoric stress vector
C
      STNORM = SQRT( DEVHLT**2 + DEVVLT**2 + (SIGKK/3.)**2 )
C
C     Calculate yield surface size
C
      SIGBAR = YIELD + H * EPLO
C
C     Determine if stress increment is elastic
C
      IF ( (SIGBAR - SQRT(1.5)*STNORM) .GT. 0. ) THEN
        SHL = SHLT
        SVL = SVLT
        DEPL = 0.
        RETURN
      END IF
C
C     Scale the stresses back to the yield surface.
C
      SCALE = SIGBAR / (SQRT(1.5) * STNORM)
```

```
      DEVHLT = SCALE * DEVHLT
      DEVVLT = SCALE * DEVVLT
      SIGKK = SCALE * SIGKK
C
C     Calculate total stresses
C
      SHL = DEVHLT + SIGKK / 3.
      SVL = DEVVLT + SIGKK / 3.
      DSIGKK = SHL + SVL - (SHLO + SVLO)
C
C     Find the change in the effective plastic strain.
C
      BULK = E / (3. * (1. - 2. * ENU))
      G2 = E / (1. + ENU)
C       Compute change in deviatoric strains :
      DELEH = DEPSH - DSIGKK / (9. * BULK)
      DELEV = DEPSV - DSIGKK / (9. * BULK)
      DELEZ = -DELEH - DELEV
C       Compute change in deviatoric stresses :
      DDEVH = DEVHLT - (SHLO - (SHLO + SVLO) / 3.)
      DDEVV = DEVVLT - (SVLO - (SHLO + SVLO) / 3.)
C       Compute plastic strain components
      EPLH = EPSH - (SHL / E - ENU * SVL / E)
      EPLV = EPSV - (SVL / E - ENU * SHL / E)
      EPLZ = -EPLH - EPLV
C       Calculate change in equivalent plastic strain :
      DEPL = SQRT ( (DELEH - DDEVH / G2)**2 + (DELEV - DDEVV / G2)**2 +
     *              (DELEZ + DSIGKK / 3. / G2)**2 )
      DEPL = DEPL * SQRT(2./3.)
      RETURN
      END
```

Distribution:

U. S. Government Printing Office
Receiving Branch (Attn: NRC Stock)
8610 Cherry Lane
Laurel, MD 20707 (500 copies for R1, RD)

US Nuclear Regulatory Commission
Engineering Branch
5650 Nicholson Lane
Rockville, MD 20852
Attn: J. F. Costello (20 copies)
H. L. Graves

US Department of Energy
Office of Nuclear Energy
Mail Stop B-107
NE-540
Washington, DC 20545
Attn: A. Millunzi
Bernard J. Rock
D. Giessing (3 copies)

CBI NaCon, Inc.
800 Jorie Boulevard
Oak Brook, IL 60521
Attn: Thomas J. Ahl

Wilfred Baker Engineering
218 E. Edgewood Pl.
P. O. Box 6477
San Antonio, TX 78209
Attn: Wilfred E. Baker

William C. Black
2650 Woodside Road
Bethlehem, PA 18017

Wiss, Janney, Elstner Assoc., Inc.
330 Pfingsten Road
Northbrook, IL 60062
Attn: Ted M. Brown

Battelle Columbus Laboratories
505 King Avenue
Columbus, Ohio 43201
Attn: Richard Denning

Bechtel Power Corporation
12400 E. Imperial Highway
Norwalk, CA 90650
Attn: Asadour H. Hadjian

Bechtel Power Corp.
15740 Shady Grove Rd.
Gaithersburg, MD 20877
Attn: T. E. Johnson
K. Y. Lee (2 copies)

1245 Newmark CE Lab
University of Illinois
208 N. Romine
MC-250
Urbana, IL 61801
Attn: Prof. Mete A. Sozen

Stevenson & Associates
9217 Midwest Ave.
Cleveland, Ohio 44125
Attn: John D. Stevenson

United Engineers & Constructors, Inc.
30 S. 17th St.
Philadelphia, PA 19101
Attn: Joseph J. Ucciferro

Electrical Power Research Institute
3412 Hillview Avenue
PO Box 10412
Palo Alto, CA 94304
Attn: H. T. Tang, Y. K. Tang
Raf Sehgal, J. J. Taylor,
W. Loewenstein (5 copies)

School of Civil & Environ. Engr.
Hollister Hall Cornell University
Ithaca, NY 14853
Attn: Professor Richard N. White

NUTECH
225 N. Michigan Ave.
16th Floor
Chicago, Illinois 60601
Attn: John Clauss

Iowa State University
Department of Civil Engineering
420 Town Engineering Bldg.
Ames, IA 50011
Attn: L. Greimann (20 copies)

TVA
400 Commerce Ave.
Knoxville, TN 37902
Attn: D. Denton, W9A18

Los Alamos National Laboratories
PO Box 1663
Mail Stop M576
Los Alamos, NM 87545
Attn: C. Anderson

EQE Inc.
3300 Irvine Aveune
Suite 345
Newport Beach, CA 92660
Attn: M. K. Ravindra

University of Illinois
Dept. of Civil Engineering
Urbana, IL 61801
Attn: C. Siess

EBASCO Services, Inc.
Two World Trade Center
New York, NY 10048
Attn: Robert C. Iotti

EG&G Idaho
Willow Creek Bldg. W-3
PO Box 1625
Idaho Falls, ID 83415
Attn: B. Barnes, T. L. Bridges
(2 copies)

Sargent & Lundy Engineers
55 E Monroe St.
Chicago, IL 60603
Attn: A. Walser
P. K. Agrawal (2 copies)

General Electric Company
175 Curtner Ave.
San Jose, CA 95125
Attn: J. E. Love, E. O. Swain,
D. K. Henrie, R. Gou (4 copies)

Westinghouse Electric Corp.
Waltz Mill Site
Box 158
Madison, PA 15663
Attn: Vijay K. Sazawal

R. F. Reedy, Inc.
236 N Santa Cruz Ave.
Los Gatos, Ca 95030

Quadrex Corporation
1700 Dell Ave.
Campbell, CA 95008
Attn: Quazi A. Hossain

ANATECH International Corp.
3344 N. Torrey Pines Court
Suite 320
LaJolla, CA 92037
Attn: Y. R. Rashid

Oak Ridge National Laboratory
PO Box Y
Oak Ridge, TN 37830
Attn: Steve Hodge

Brookhaven National Laboratory
Building 130
Upton, NY 11973
Attn: C. Hofmayer,T. Pratt
M. Reich (3 copies)

Argonne National Laboratory
9700 South Cass Avenue
Argonne, IL 60439
Attn: J. M. Kennedy,
R. F. Kulak,
R. W. Seidensticker (3 copies)

Tennessee Valley Authority
400 Summit Hill Rd.
W9D24C-K
Knoxville, Tennessee 37902
Attn: Nathaniel Foster

University of Wisconsin
Nuclear Engineering Dept.
Madison, WI 53706
Attn: Prof. Michael Corradini

Brookhaven National Laboratory
Building 820M
Upon, NY 11973
Attn: Ted Ginsberg

Dept. of Chemical & Nuclear Engineering
University of California Santa Barbara
Santa Barbara, CA 93106
Attn: T. G. Theofanous

Institut für Mechanik
Universität Innsbruck
Technikerstr. 13
A-6020 Innsbruck
Austria
Attn: Prof. G. I. Schuëller

Nuclear Studies & Safety Dept.
Ontario Hydro
700 University Avenue
Toronto, Ontario
M5G 1X6
Canada
Attn: W. J. Penn

University of Alberta
Dept. of Civil Engineering
Edmonton, Alberta
Canada T6G 2G7
Attn: Prof. D. W. Murray

Commissariat a L'Energie Atomique
Centre d'Etudes Nucleaires de Saclay
F-91191 Gif-Sur-Yyette Cedex
France
Attn: M. Livolant, P. Jamet (2 copies)

Institut de Protection et de
Surete Nucleaire
Commissariat a l'Energie Atomigue
F-92660 Fontenay-aux-Roses
France
Attn: M. Barbe

Kernforschungszentrum Karlsruhe GmbH
Postfach 3640
D-7500 Karlsruhe
Federal Republic of Germany
Attn: R. Krieg, P. Gast (2 copies)

Lehrstuhl fuer Reakordynamik
und Reaktorsicherheit
Technische Universitaet Muenchen
D-8046 Garching
Federal Republic of Germany
Attn: Prof. H. Karwat

Staatliche Materialpruefungsanstalt (MPA)
University of Stuttgart
Pfaffenwaldring 32
D-7000 Stuttgart 80 (Vaihingen)
Federal Republic of Germany
Attn: Prof. K. F. Kussmaul

Gesellschaft fuer Reaktorsicherheit
Schwertnergasse 1
D-5000 Köln 1
Federal Republic of Germany
Attn: H. Schulz, A. Hoefler,
F. Schleifer (3 copies)

Kraftwerk Union AG
Hammerbacherstr. 12-14
D-8520 Erlangen
Federal Republic of Germany
Attn: M. Hintergräber

Ente Nazionale per l'Energia Elettrica
v. le Regina Margherita, 137
Rome
Italy
Attn: Francesco L. Scotto

ISMES
Viale Giulio Cesare 29
I-24100 Bergamo
Italy
Attn: A. Peano

ENEA-DISP
ACO-CIVME
Via Vitaliano Brancati, 48
I-00144 Roma
Italy
Attn: Giuseppe Pino

Nuclear Equipment Design Dept.
Hitachi Works, Hitachi, Ltd.
3-1-1 Saiwai-Cho
Hitachi-Shi
Ibaraki-ken
Japan
Attn: O. Oyamada

Division of Technical Information
Japan Atomic Energy Research Institute
2-2, Uchisaiwai-cho 2-chome
Chiyoda, Tokyo 100
Japan
Attn: Jun-ichi Shimokawa

University of Tokyo
Institute of Industrial Science
22-1, Roppongi 7
Minatu-ku, Tokyo
Japan
Attn: Prof. H. Shibata

Civil Engineering Laboratory
Central Research Institute of
Electric Power Industry
1646 Abiko Abiko-Shi Chiba
Japan
Attn: Yukio Aoyagi

Kajima Corporation
No. 1-1, 2-Chome Nishishinjuku
Shinjuku-ku
Tokyo 160
Japan
Attn: K. Umeda

Muto Institute of Structural Mechanics
Room 3005 Shinjuku Mitsui Building
Shinjuku-ku
Tokyo, 163
Japan
Attn: Tadashi Sugano

Nuclear Power Engineering Test Center
6-2, 3-Chome, Toranomor
Minatoku
Tokyo 105
Japan
Attn: Yoshio Tokumaru

Japan Atomic Energy Research Inst.
Tokai-Mura, Ibaraki-Ken 319-11
Japan
Attn: Kunihisa Soda
Toshikuni Isozaki (2 copies)

Shimizu Construction Co., Ltd.
No. 4-17, Etchujima 3-Chome
Koto-Ku
Tokyo 135
Japan
Attn: Toshihiko Ota

Shimizu Construction Co., Ltd.
No. 18-1, Kyobashi 1-Chome
Chuo-ku
Tokyo 104
Japan
Attn: Toshiaki Fujimori

Korea Advanced Energy Research Inst.
P. O. Box 7
Cheong Ryang
Seoul
Korea
Attn: Pilsoon Han

Universidad Politecnica
Escuela Tecnica Superior
de Ingenieros Industriales
Madrid
Spain
Attn: Agustin Alonso

Studsvik Energiteknik AB
S-611 82 Nyköping
Sweden
Attn: Kjell O. Johansson

Swedish State Power Board
Nuclear Reactor Safety
S-162 87 Vällingby
Sweden
Attn: Hans Cederberg
Per-Eric Ahlström
Ralf Espefaelt (3 copies)

Swiss Federal Institute of Technology
Institute of Structural Engineering
ETH-Hoenggerberg, HIL
CH-8093 Zurich
Switzerland
Attn: W. Ammann

Motor-Columbus Consulting Engineers, Inc.
Parkstrasse 27
CH-5401 Baden
Switzerland
Attn: K. Gähler, A. Huber
A. Schopfer (3 copies)

EIR (Swiss Federal Institute for
Reactor Research)
CH-5303 Wuerlingen
Switzerland
Attn: O. Mercier
P. Housemann (2 copies)

Swiss Federal Nuclear Safety Inspectorate
Federal Office of Energy
CH-5303 Wuerenlingen
Switzerland
Attn: S. Chakraborty

Swiss Federal Institute of Technology
Chemin de Bellerive 32
CH-1007 Lausanne
Switzerland
Attn: Prof. F. H. Wittmann

Elektrowatt Ingenieurunternehmung AG
Bellerivestr. 36
CH-8022 Zürich
Switzerland
Attn: John P. Wolf

Institute of Nuclear Energy Research
P. O. Box 3
Lung-Tan
Taiwan 325
Republic of China
Attn: Sen I Chang

Atomic Energy Establishment
Winfrith
Dorchester Dorset
DT2 8DH
United Kingdom
Attn: Peter Barr

Atomic Energy Authority
Safety and Reliability Directorate
Wigshaw Lane
Culcheth
Warrington WA3 4NE
United Kingdom
Attn: D. W. Phillips

HM Nuclear Installation Inspectorate
St. Peter's House
Stanley Precinct
Bootle L20 3LZ
United Kingdom
Attn: R. J. Stubbs

Northern Illinois University
Mechanical Engineering Dept.
DeKalb, IL 60115
Attn: A. Marchertas

Taylor Woodrow Construction Limited
345 Ruislip Road
Southall, Middlesex
UB1 2QX
United Kingdom
Attn: Carl C. Fleischer
Richard Crowder (2 copies)

Central Electricity Generating Board
Barnett Way
Barnwood, Gloucester
GL4 7RS
United Kingdom
Attn: J. Irving

Central Electricity Generating Board
Booths Hall
Chelford Road
Knutsford, Cheshire
WA16 8QG
United Kingdom
Attn: Carl Lomas

City College of New York
Dept. of Civil Engineering
140 Street and Convent Ave.
New York, NY 10031
Attn: C. Costantino

1510 J. W. Nunziato
1520 C. W. Peterson
1521 R. D. Krieg
1521 J. R. Weatherby (5)
1530 L. W. Davison
1550 R. C. Maydew
3141 S. A. Landenberger (5)
3151 W. L. Garner
6400 D. J. McCloskey
6410 N. R. Ortiz
6413 E. D. Gorham-Bergeron
6420 J. V. Walker
6440 D. A. Dahlgren
6442 W. A. von Riesemann (22)
6442 D. B. Clauss
6442 D. S. Horschel
6442 D. L. Lambert
6442 M. B. Parks
6447 M. B. Bohn
6500 A. W. Snyder
8024 P. W. Dean

NRC FORM 335 (2-84) NRCM 1102, 3201, 3202

U.S. NUCLEAR REGULATORY COMMISSION

BIBLIOGRAPHIC DATA SHEET

SEE INSTRUCTIONS ON THE REVERSE

1 REPORT NUMBER (Assigned by TIDC, add Vol. No., if any)

NUREG/CR-4969
SAND87-1670

2 TITLE AND SUBTITLE

Axisymmetric Analysis of a 1:6-Scale Reinforced Concrete Containment Building Using a Distributed Cracking Model for the Concrete

3 LEAVE BLANK

4 DATE REPORT COMPLETED

MONTH	YEAR
August	1987

5 AUTHOR(S)

Joe R. Weatherby

6 DATE REPORT ISSUED

MONTH	YEAR
October	1987

7 PERFORMING ORGANIZATION NAME AND MAILING ADDRESS (Include Zip Code)

Sandia National Laboratories
Albuquerque, New Mexico 87185

8 PROJECT/TASK/WORK UNIT NUMBER

9 FIN OR GRANT NUMBER

FIN A1401

10 SPONSORING ORGANIZATION NAME AND MAILING ADDRESS (Include Zip Code)

Division of Engineering Technology
Office of Nuclear Regulatory Research
U.S. Nuclear Regulatory Commission
Washington, D.C. 20555

11a TYPE OF REPORT

Topical

b PERIOD COVERED (Inclusive dates)

January 1987 - August 1987

12 SUPPLEMENTARY NOTES

13 ABSTRACT (200 words or less)

Results of axisymmetric structural analyses of a 1:6-scale model of a reinforced concrete nuclear containment building are presented. Both a finite element shell analysis and a simplified membrane analysis were made to predict the structural response and ultimate pressure capacity of the model. Analytical results indicate that the model will fail at an internal pressure of 187 psig when the stress level in the hoop reinforcement at the midsection of the cylinder exceeds the ultimate strength of the bar splices.

14 DOCUMENT ANALYSIS - a KEYWORDS/DESCRIPTORS

b IDENTIFIERS/OPEN-ENDED TERMS

15 AVAILABILITY STATEMENT

16 SECURITY CLASSIFICATION

(This page)
Unclassified

(This report)
Unclassified

17 NUMBER OF PAGES

18 PRICE

☆ U.S. GOVERNMENT PRINTING OFFICE: 1988-579-048/61213